

AD-A120 581

ACTA MECHANICA SINICA (SELECTED ARTICLES)(U) FOREIGN  
TECHNOLOGY DIV WRIGHT-PATTERSON AFB OH G LING ET AL.

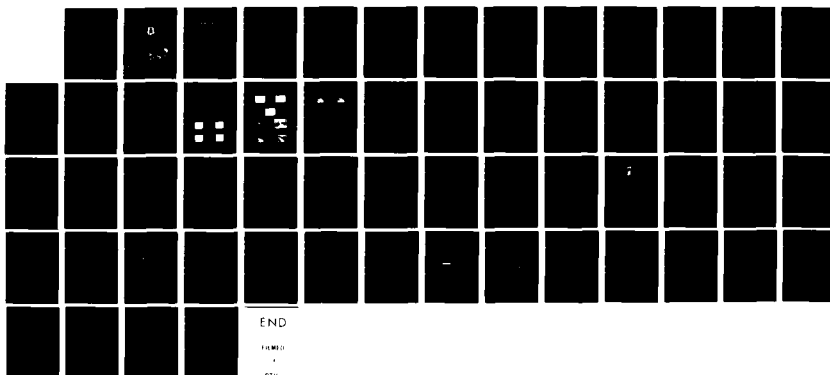
1/1

19 AUG 82 FTD-ID(RS)T-0619-82

UNCLASSIFIED

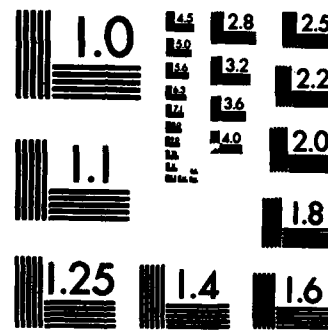
F/G 20/4

NL



END

FMU/1  
DTK



MICROCOPY RESOLUTION TEST CHART  
NATIONAL BUREAU OF STANDARDS-1963-A

AD A120581

FTD-ID(RS)T-0619-82

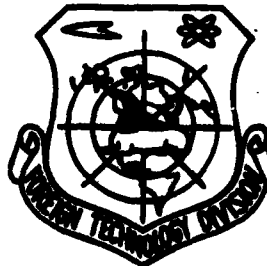
9

## FOREIGN TECHNOLOGY DIVISION



ACTA MECHANICA SINICA

(Selected Articles)



Approved for public release;  
distribution unlimited.

DTIC FILE COPY



82 10 21 050

## EDITED TRANSLATION

FTD-ID(RS)T-0619-82

19 August 1982

MICROFICHE NR: FTD-82-C-001118

ACTA MECHANICA SINICA (Selected Articles)

English pages: 54

Source: Acta Mechanica Sinica, Nr. 1, 1982,  
pp. 18-25; 34-41; 55-62; 97-103; App 1 and 2

Country of origin: China

Translated by: LEO KANNER ASSOCIATES  
F33657-81-D-0264

Requester: FTD/TQTA

Approved for public release; distribution unlimited.

THIS TRANSLATION IS A RENDITION OF THE ORIGINAL FOREIGN TEXT WITHOUT ANY ANALYTICAL OR EDITORIAL COMMENT. STATEMENTS OR THEORIES ADVOCATED OR IMPLIED ARE THOSE OF THE SOURCE AND DO NOT NECESSARILY REFLECT THE POSITION OR OPINION OF THE FOREIGN TECHNOLOGY DIVISION.

PREPARED BY:

TRANSLATION DIVISION  
FOREIGN TECHNOLOGY DIVISION  
WPAFB, OHIO.

FTD -ID(RS)T-0619-82

Date 19 Aug 19 82

## Table of Contents

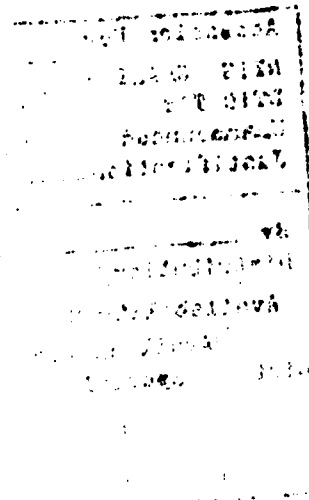
Graphics Disclaimer . . . . .	ii
The Secondary Vortex and the Process of the Formation of the Karman Vortex, by <u>Ling Guocan</u> , and <u>Yin Xieyuan</u> . . . . .	1
Numerical Computation of the Viscous Compressible Flow in Turbomachinery. (II) Computation of Axisymmetric Flow in the Rotor, by <u>Jiang Jinliang</u> . . . . .	16
Partial Differential Equations Satisfied by Stream Functions in Three Dimensional Turbomachinery Flow and the Finite element Solution, by <u>Li Kaitai</u> , and <u>Huang Aixiang</u> . . . . .	29
Iridium Electrostatic Probe and its Application in a High Temperature Wind Tunnel, by <u>Wang Boyi</u> . . . . .	42



Accession For	
NTIS GRA&I	<input checked="" type="checkbox"/>
DTIC TAB	<input type="checkbox"/>
Unannounced	<input type="checkbox"/>
Justification	
By	
Distribution/	
Availability Codes	
Dist	Avail and/or Special
A	

#### **GRAPHICS DISCLAIMER**

**All figures, graphics, tables, equations, etc. merged  
into this translation were extracted from the best  
quality copy available.**



## THE SECONDARY VORTEX AND THE PROCESS OF THE FORMATION OF THE KARMAN VORTEX

Ling Guocan, and Yin Xieyuan

Ling of the Institute of Mechanics, Chinese Academy of Sciences; and Yin of the Department of Modern Physics, China University of Science and Technology

Submitted October 1980

A method is used in which the discrete vortex model is combined with boundary layer theory; the boundary layer separation and the rear shear layer separation are simultaneously taken into account. The authors studied and formulated the formation, growth and effect of a secondary vortex in the near wake of a circular cylinder, which is started by impulse from rest and subsequently moves with constant velocity; they also studied the immediate cause leading to the instability of the motion of symmetric main vortices and described the process of the formation of the Karman vortex. Those numerical results are given.

In this paper, the authors suggest that under the effect of a secondary vortex while the symmetric main vortices vary from the state of a vorticity supplement into free vortices, the final state has no further vorticity supplement. The condition that leads to instability of the motion of symmetric main vortices exists. Then under the action of a small disturbance a fluctuating motion may be produced and further development leads to Karman vortex motion.

In the present work the flow is considered to be laminar and the Reynolds number is high. The results given in the present work look very much like the observed features in flow field visualization.

## I. Foreword

The unsteady motion of a suddenly moved circular cylinder is a classic and complex problem. With a high Reynolds number and laminar flow with lengthening of time, these complicated flow phenomena include unsteady separation of boundary layers, formation and growth of symmetric vortices, asymmetric motion of vortices, formation of a Karman vortex, vortex street motion, and others. Many years' theoretical study brought about very successful analysis of the flow characteristics within a very short time after start of motion and of the characteristics of vortex street motion after a longer time of motion; fundamentally, the study solves the problem of an unsteady boundary layer under the condition of potential flow solution. However, for the state of motion in the intermediate stage, that is the stage from beginning of separation to the formation of the Karman vortex, a result is still not available to satisfy the theoretical analysis except a few purely numerical solutions of the N-S equations. In particular, the following three problems have not been clarified: (1) the formation and growth of the secondary vortex and vortex pair as well as their effect on the flow and main vortex; (2) direct cause and condition of motion instability in the growth process of symmetric main vortices; and (3) the formation process of the Karman vortex. Theoretically, there has not been a perfect and satisfactory explanation and description.

Modern experiments utilize a delicate flow field display technique to conduct some research on the separation process of secondary and main vortices. For the main work, refer to papers [1-4]. Paper [1] was the first observation of the existence of the secondary vortex, and it pointed out that  $Re=U_\infty d/\nu > 550$  is the condition of emergence of the secondary vortex. In paper [1], there is the observation of existence of a pair of secondary vortices and the paper derives diagrams of formation and breaking up of a secondary vortex. The experiment in paper [2] clearly indicates the formation process and variation of the main vortex near the wake when the Re number is  $10^2$  to  $2 \times 10^3$  with formation and variation of a secondary vortex. It was observed that interruption may occur in the main vortex layer at a certain instant in the growth and variation process of secondary and main vortices when  $Re > 10^3$ ; no interruption occurs in the main vortex layer when  $Re < 10^3$ . In paper [2], it was pointed out that the state of the secondary vortex is closely

related to the growth and destruction of main vortex. In paper [3] (1979), the experimental results when the Re number is 30-5000 were reported. When  $Re > 500$ , one or more secondary vortices exist and have been observed near the region of separation of the main stream. The experiments revealed flow variation near the vortex in the formation process of a secondary vortex. These experiments enrich the researchers' knowledge of the evolution of vortex motion behind a cylinder, which carries out an unsteady motion; this is helpful in regime analysis of the flow process. However, at present there is neither a corresponding report on the theoretical analysis, nor does the theoretical calculation result match the experimental result.

Theoretically, an accurate method of numerical solution was used to calculate the secondary vortex; the main work was done in papers [5-8]. In paper [5], a numerical solution was given to the N-S equation under a high Reynolds number ( $4 \times 10^4$ ); the formation of a secondary vortex was obtained behind the cylinder. In papers [6-8], calculations were conducted for a medium Reynolds number (Re about 500); only the structure of a single secondary vortex was derived with a blurred diagram of slightly bulging streamlines in the local region. There is no consistent result in experimental observations. The results of numerical calculation only matched some experimental displays, especially in formation and growth of a secondary vortex. Besides, these numerical solutions clearly describe the variation process of the flow only with difficulty. In paper [9], a model of a divergent vortex was used and consideration was given to the effect on flow of separation of the rear shear layer. The secondary divergent vortex obtained in the calculation enters the lower stream of the wake with the structure of the vortex blurred. The paper did not conduct a theoretical analysis of the rear shear layer and its separation; only an empirical formula of the separation point following the calculation was given. Hence, the theoretical study conducted achieved only a preliminary result.

This paper intends to use a method of combining the potential flow theory of a divergent vortex and the boundary layer theory. Simultaneous consideration is given to the model of a divergent vortex separated from the boundary layer and the rear shear layer in order to study and calculate the formation, growth and effect of secondary vortices during the process of unsteady motion of a cylinder. The

direct cause and conditions are also studied on unsteady motion of the main vortices, and the process of formation of a Karman vortex is analyzed. The paper considers the situation of uniform-speed straight-line motion after a cylinder suddenly moves in an incompressible, laminar flow with high Reynolds number.

## II. Theoretical Analysis

### 1. Model of divergent vortex

In paper [10], the authors described in detail the model of a divergent vortex. Simultaneous consideration was given to the divergent-vortex model separated from the boundary layer and the rear shear layer; these considerations can be generalized as follows: the boundary layer is relatively thin with a high Reynolds number; the stage beginning with separation to the formation of the Karman vortex is the initial stage of the entire unsteady motion; in this stage, a region of a relatively thin shear layer of circulation flow is formed gradually, including a rear stationary point; and the viscous effect is mainly concentrated in these thin layers. From the beginning of the motion to the instant that a certain characteristic occurs, the boundary layer begins to separate. At a certain time, under certain conditions the shear layer also begins to separate. The separation points vary with time and the vortices of the boundary layer and rear shear layer move to the lower-stream wake through the respective separation points. The continuous motion process of this vorticity can be substituted by the constant separation and motion of a divergent, nonviscous potential vortex with a certain intensity and formation at certain time intervals. However, there are reverse directions between the divergent vortex from the shear layer and the divergent vortex formed at the boundary layer. The motion of the divergent vortex is determined by the local potential-flow field. The potential-flow field is formed by superposition of two parts: a constantly increased divergent vortex and the potential-flow field of flow winding around the straight uniform-flow cylinder. With time variation, flow fields corresponding to different time intervals are then obtained. The pressure at the object surface and velocity distribution are new external-edge conditions of the boundary layer and rear shear layer. Under these conditions, separation of the boundary layer and rear shear layer is again calculated to determine the new separation point and divergent vortex, forming a new flow field of the entire potential flow. By repeated calculation in such a way,

the divergent-vortex model of unsteady initial motion with high Reynolds number is described for a cylinder with consideration of mutual actions among boundary layer, near-wake flow and external potential flow.

## 2. Flow field of nonviscous potential flow

If we assume that  $W(Z)$  is the compound potential of potential-flow field,  $\theta_k$  and  $r_k$  are respectively the motion positions of the  $k$ -th vortex at any instant of the polar coordinate system, then in paper [10] the equations are as follows:

$$W(Z) = Z + \frac{1}{Z} + \sum_{n=1}^N i \Gamma_n \ln \frac{Z - \bar{Z}_n}{Z - Z_n} \quad (1)$$

$$\frac{dr_k}{dt} = \frac{r_k^2 - 1}{r_k^2} \cos \theta_k + \sum_{n=1}^N \Gamma_n r_n \sin(\theta_k - \theta_n) S_1^{-1} - \sum_{n \neq k}^N \Gamma_n r_n \sin(\theta_k - \theta_n) S_2^{-1}$$

$$\frac{d\theta_k}{ds} = - \frac{r_k^2 + 1}{r_k^2} \sin \theta_k - \sum_{n=1}^N \Gamma_n [r_k r_n - r_n \cos(\theta_k - \theta_n)] (r_k S_1)^{-1} + \sum_{n \neq k}^N \Gamma_n [r_k - r_n \cos(\theta_k - \theta_n)] (r_k S_2)^{-1} \quad (2)$$

$$S_1 = 1 + r_k^2 r_n^2 - 2 r_k r_n \cos(\theta_k - \theta_n)$$

$$S_2 = r_k^2 + r_n^2 - 2 r_k r_n \cos(\theta_k - \theta_n)$$

$$n = 1, 2, \dots, N, \quad k = 1, 2, \dots, N$$

In the equations,  $Z_n$  and  $\Gamma_n$  are respectively the position and intensity of the  $n$ -th divergent vortex.  $N$  is the total number of all divergent vortices, and is also the summation of total divergent vortices formed with separation of boundary layer and the total divergent vortices formed by separation from the rear shear layer.

Obviously,  $N$  varies with time.  $Z_n$  is also a function of time  $t$ .  $\Gamma_n$  is determined by vorticity at the separation point of the boundary layer or rear shear layer.

The equations of pressure distribution  $C_p$ , velocity distribution  $V_B$  and resistance coefficient  $C_p$  at the object surface are, respectively, [10]:

$$\begin{aligned}
 C_p(\theta, t) &= 1 - V_1 + 2 \sum_{n=1}^N \Gamma_n \frac{\partial}{\partial t} (\theta_{n+1}^{**} - \theta_n^*) \\
 V_n(\theta) &= -2 \sin \theta + \sum_{n=1}^N \Gamma_n \frac{1 - r_n^2}{1 - 2r_n \cos(\theta - \theta_n) + r_n^2} \\
 C_D &= -4\pi \sum_{n=1}^N \Gamma_n \left[ \left(1 + \frac{1}{r_n^2}\right) \frac{dr_n}{dt} \sin \theta_n + \left(r_n - \frac{1}{r_n}\right) \frac{d\theta_n}{dt} \cos \theta_n \right] \\
 \theta_{n+1}^{**} &= \tan^{-1} \frac{r_n \sin \theta - \sin \theta_n}{r_n \cos \theta - \cos \theta_n} \\
 \theta_n^* &= \tan^{-1} \frac{\sin \theta - r_n \sin \theta_n}{\cos \theta - r_n \cos \theta_n}
 \end{aligned} \tag{3}$$

### 3. Separation of boundary layer

The flow closely contacting the object surface should satisfy the unsteady two-dimensional incompressible boundary layer equation and the corresponding initial boundary-value conditions; the boundary conditions are given by the above-mentioned distribution of velocities of potential flow. Hence, the internal layer, external layer, and near wake are mutually affected. In the divergent vortex model, the main interest is the variation of separation point with time. Hence, the problem can be regarded as the coupling solution of the separation point of an unsteady boundary layer. Since this paper emphasizes the problem of the secondary vortex, as the preliminary description of this problem it is expected to reduce the calculation amounts and complexity during calculation. Hence, the variation in separation point of the boundary layer uses an empirical-relationship equation in paper [10] written by the authors and for the time being the coupling solution is not given. (This empirical equation is derived from an accurate numerical solution. At the same time, the calculated numerical results of the boundary-layer separation point and the rear shear-layer separation point will be given in another paper.)

$$\theta_s = 98.0 - 58.0 \exp[-1.1968(t - 0.65)] \tag{4}$$

The above equation indicates the variation rule with time of a separation point for actual unsteady flow of a cylinder. The initial separation time is  $t=0.65$  and  $\theta_s = 40^\circ$ .

#### 4. Separation of rear shear layer

In paper [10] a detailed analysis was given of the flow of unsteady motion at its initial stage without considering the situation of the secondary vortex, giving the variation rule for object-surface flow characteristics, such as distributions of object-surface pressures and velocities. On this basis, this paper conducts another step of regime analysis for the rear shear layer formed in the initial stage; some reasonable assumptions are made.

We can see from paper [10], on the formation and growth of the symmetric main vortices, that at a certain instant a circulating flow region appears in the vicinity of the object surface behind the cylinder. With lengthening of time, the range of the circulating region gradually expands and includes the rear stationary points. At that time, in the vicinity of the object surface a rear shear layer including a rear stationary point is formed. From the rear stationary point, the circulating flow along the object surface is in the process of velocity reduction and pressure increase within a considerable range. This paper assumes that in the initial stage of this unsteady motion, the shear layer has the boundary layer characteristic of laminar flow. Under the persistent (non-instantaneous) action of a reverse pressure gradient, boundary-layer separation occurs. On the cylindrical object surface in the circulating flow region, the position of the minimum pressure point is considered to separate where it is not continuously moving upward along the cylindrical surface. At that time, we assume that the variation of the rear shear layer tends toward a quasi-steady state. This paper uses the separation-point calculation method (on the rear shear layer) for the boundary layer of Stratford laminar flow. At the rear separation point, the following relationship is satisfied [10]:

$$\begin{aligned}
 & \left[ C_p' \left( x' \frac{dC_p'}{dx'} \right) \right]_{r_s} = 0.0104 \\
 & x' = \theta - \theta_s \\
 & \theta_s = \theta_{p \min(r)} - \int_0^{\theta_{p \min(r)}} \left( \frac{V_x}{V_{x_s}^*} \right)^2 d\theta \\
 & C_p' = \frac{p - p_{\min(r)}}{\frac{1}{2} \rho (V_{x_s}^*)^2}
 \end{aligned} \tag{5}$$

In the equation,  $p_{\min(r)}$  is the minimum pressure value on the cylindrical surface in the circulating flow region;  $\theta_{p \min(r)}$  is the position of this point departing

from the rear stationary point, and  $V_B^*$  is the velocity of external-edge potential flow of the corresponding object surface.

### 5. Intensity of divergent vortex

The intensity of the divergent vortex should equal the vorticity of the boundary layer, which is within one time step from the separation point; the intensity can be indicated by the velocity of potential flow of the object surface. Let  $\Gamma_n^f$  and  $\Gamma_n^r$  indicate, respectively, intensities of divergent vortices coming from the boundary layer and rear shear layer;  $V_{Bfs}$  and  $V_{Brs}$  are, respectively, velocities of external-edge potential flows corresponding to the separation point of the boundary layer and the separation point of the shear layer; and  $\Delta t$  is the length of the time step during calculation. Then [10]

$$\begin{aligned}\Gamma_n^f &= \frac{1}{4\pi} V_{Bfs}^2 \Delta t \\ \Gamma_n^r &= -\frac{1}{4\pi} V_{Brs}^2 \Delta t\end{aligned}\quad (6)$$

### III. Brief Description of Calculations

Equations (2), (4), (5) and (6) are simultaneous equations for determining motions and intensities of  $N$  divergent vortices. The simultaneous differential equations are numerically solved using the Runge-Kutta method of varying the number of equations. In calculations, attention should be paid to selecting a unit time step. If a time step is too large, the use of the "divergent" method to simulate vorticity or continuous motion of vorticity will not lead to accurate results. If the time step is too small, the interval of divergent vortices will be very dense, and then singularities will appear while using the theory of potential flow to calculate the induction speed; in addition, the computer time required will be considerable. The paper refers to paper [10] to finally select 0.125 as the length of the time step. For the time of initial separation, the paper also refers to paper [10] by selecting  $t=0.65$ . The newborn vortex is situated at  $\theta_s=40^\circ$ . Later on, for each step length two divergent vortices increase with increase of six equations. (When equation (1) is used to calculate the compound potential, the contribution of the display-image vortex is included.)

At  $t=2.650$  the calculation begins on the separation of the rear shear layer. Later on, for each step length four divergent vortices increase with the addition of 12 equations. When numerical calculation is conducted on each step length of equations (2) to (6), all divergent vortices separated from the boundary layer and all divergent vortices separated from the rear shear layer should be taken into account and numbered consecutively. After calculation, a program is used to distinguish the divergent vortex region from the rear shear layer already existing at that instant in order to obtain a clear image of the secondary vortex. At the separation point of the newborn vortex during separation, the distance (of the vortex) from the cylindrical surface should not be greater than the thickness of the boundary layer or the thickness of the shear layer. For calculation convenience, the paper selects an approximate figure,  $r_n=1.05$  [10]. The paper calculates from separation of boundary layer to  $t^4$ . In the final calculation of step length, there are 74 divergent vortices and 222 simultaneous equations, including 148 conventional differential equations. In order to save computer time and reduce internal memory storage during repeated calculations, the calculation results of the unsteady process are stored sector by sector, and the compiled program can have an arbitrary number of vortices as the initial condition to begin the calculation. By using equation (3), the velocity and pressure distributions along the object surface and resistance coefficient can be obtained.

#### IV. Results

As revealed by analysis and theoretical calculation, in the unsteady process of a cylinder after its sudden start and subsequently maintaining uniform velocity, rear shear layers are formed under the influence of induction by a pair of main vortices behind the cylinder. Under the persistent action of a reverse pressure gradient, the rear shear layers are separated and the reverse-direction secondary divergent vortex is formed. With lengthening of time, the secondary divergent vortex forms a secondary vortex surface within a limited range; the vorticity is gradually accumulated and intensified. The formation and growth of the secondary vortex causes apparent variation of flow in the vicinity, and apparently affects the motion of the divergent vortex separated from the boundary layer of the incoming flow, thus affecting the motion of vorticity separated from the boundary layer.

and the accumulation of vorticity of symmetrical main vortices. When this process develops to a certain degree, the surface of the main vortex will break up. At the broken terminal, the surface of the main vortex again rolls up, becoming the vortex surface of the third vortex. Within a limited space range, this third vortex and the secondary vortex form a secondary vortex pair. At another broken terminal, the main vortices become a pair of free vortices almost without a vorticity supplement. In paper [11], the symmetrically arranged free vortex pair has been proved; its motion is unsteady. Hence, the symmetrical main vortices vary from a non-free vortex with vorticity supplement to free vortices without vorticity supplement; this means that the motion of symmetrical vortices has unsteady conditions. Due to the effect of the secondary vortex, the main vortices become free vortices; this is the direct cause of the symmetrical main vortices having unsteady motion. At that time, pulsation occurs easily with a little disturbance and asymmetrical motion begins. After the main vortices have asymmetrical motion, the secondary vortex will break up and develop into a Karman vortex.

Figure (1a to 1f) shows the partial calculation results in the paper. Since in the near wake region, within the time duration considered, the vortex motion is symmetrically developed, thus in the figure only the state of variation of the upper half of the plane is given. Figure 1a shows the situation of symmetric vortices in the near-the-wake region before separation of the rear shear layer. Within the time duration shown in Fig. 1b, there are three secondary divergent vortices and the secondary vortex surface begins to be formed. Starting from Fig. 1c, the secondary vortex is constantly intensified with more and more effect on the main vortices. The secondary vortex causes an apparent change of vorticity motion from boundary layer to lower stream and accumulation of vorticity of the main vortex. At the time instant indicated by Fig. 1c, the surface of the main vortex breaks up. Later on, the vortex surface of the broken terminal rolls up and forms a secondary vortex pair [Fig. 1f]. At that time, almost all vorticity from the boundary layer is accumulated in the newly formed third vortex. Once the main vortices become free vortices, they begin entering an unsteady state. These calculation results describe, with an image, the formation and growth of a secondary vortex, as well as the process of the main vortices becoming free vortices due to the effect of the secondary vortex. The formation process (at

the initial stage) of the Karman vortex is described with images. In paper [2], the vortex motions of the near-wake region of a cylinder with small Reynolds number ( $Re < 520$ ), medium Reynolds number ( $520 < Re < 1000$ ) and high Reynolds number ( $Re > 1000$ ) are given. The photographs (1a-1g) show results of a group (among them) of high Reynolds number ( $Re = 1220$ ). From the photographs, the growth of the secondary vortex, the breaking up of the main vortex surface, and process of formation of a secondary vortex pair (referring to photographs 1(c-d) of photo plate I) in the unsteady motion of a cylinder can be clearly seen. Later, beginning with photograph 1d, the motion of the vortex pair gradually changes into an asymmetrical situation. Photographs 2 (a to f) of photo plate I show the result of another group of experiments ( $Re = 1200$ )<sup>1)</sup>. It was observed that the growth of the secondary vortex and variation of the main vortex are the same as the process described in paper [2]. The results of analysis and calculation in the paper are very similar to these experimental results with high Reynolds number. Positions of secondary vortex pairs obtained by calculation in the paper are situated, respectively, at  $\theta \sim 41^\circ$  and  $51^\circ$ . The result is quite consistent with the positions ( $\theta \sim 40^\circ$  and  $50^\circ$ ) of secondary vortex pairs indicated in experiments.

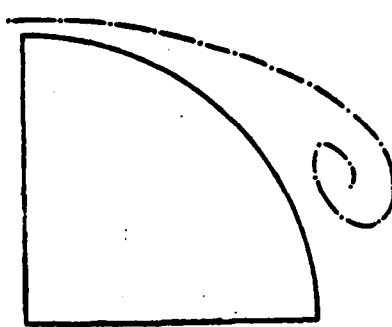


Fig. (1a)  $s = 2.6$

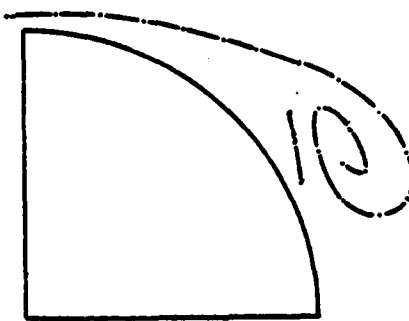


Fig. (1b)  $s = 2.9$

<sup>1)</sup>This group of photographs was selected from "Display Study of Vortices" by Matsui, Tatsuya, , Report of Japanese Fluid Dynamics Delegation's Visit to China, 1979, Beijing.

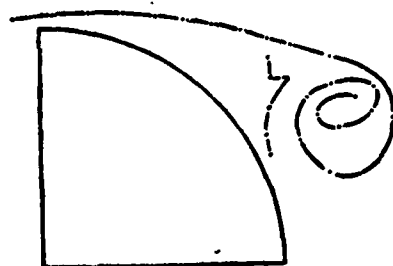


Fig. (1c)  $t = 3.4$

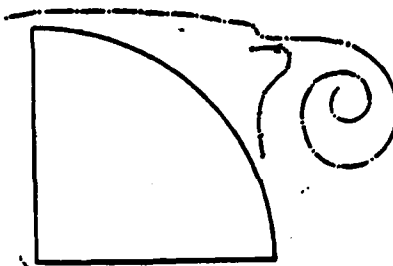


Fig. (1d)  $t = 3.63$



Fig. (1e)  $t = 3.775$

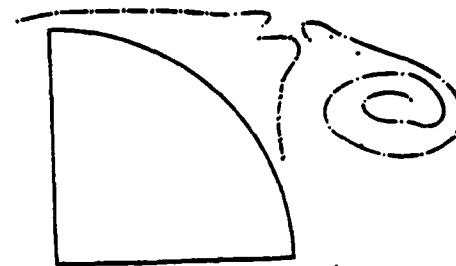


Fig. (1f)  $t = 3.9$



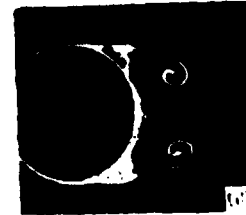
Photograph 1(a)  
 $t = 3.0$



Photograph 1(b)  
 $t = 3.4$



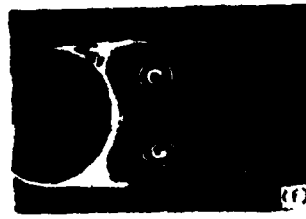
Photograph 1(c)  
 $t = 3.8$



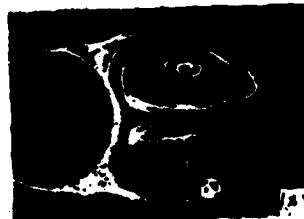
Photograph 1(d)  
 $t = 4.6$



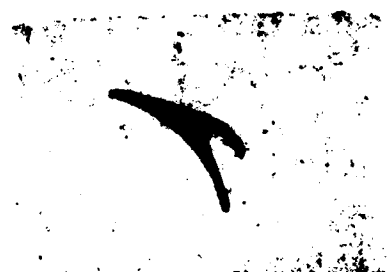
Photograph 1(e)  
 $t = 5.2$



Photograph 1(f)  
 $t = 6.2$



Photograph 1(g)  
 $t = 11.8$



Photograph 2(a)  
 $t = 1.794$



Photograph 2(b)  
 $t = 2.45$



Photograph 2(c)  
 $t = 2.75$



Photograph 2(d)  
 $t = 3.108$



Photograph 2(e)  
 $t = 3.766$



Photograph 2(f)  
 $t = 4.096$

## V. Conclusion

In this paper, simultaneous considerations are given to models of a divergent vortex with separation of the boundary layer and shear layer with analysis and calculation of a secondary near-wake vortex separated by unsteady motion of a cylinder with high Reynolds number. The paper describes the formation of a secondary vortex and the effect on main vortices, as well as the process of change from symmetrical main vortices to free vortices. The paper also raises the conditions of unsteady motion of symmetrical vortices. The evolution of flow in the process of formation of a Karman vortex is described in detail. The regime analysis of formation of the Karman vortex is provided. The formation of the Karman vortex may have different complex details with different Reynolds numbers. In this paper, consideration is given to the flow of unsteady motion of a sector of an unsteady process from a sudden start to the appearance of asymmetrical motion of the main vortices; the paper considers the conditions of high Reynolds number and laminar flow. Further study is required in theoretical calculations from the sudden appearance of asymmetrical conditions to alternate separation of main vortices and the formation of a Karman vortex row. In order to reduce the calculations, in the paper the variation rule of separation point of the boundary layer is given by an empirical relationship equation. In a later work, the authors obtained the numerical calculation results for the solution of boundary layer separation and separation coupling of the rear shear layer. In addition,

consideration of effect of a viscous vortex eye is included. Everything concerning the formation, growth and effect of the secondary vortex and the variation from main vortex to free vortex is consistent with the descriptions in the paper.

#### LITERATURE

1. Hiroyuki Honji and Sadatoshi Taneda, Unsteady Flow Past a Circular Cylinder, Journal of the Physical Society of Japan, 27, 6 (1969).
2. Hiroshi Nagata, Yutaka Kakehi, Masaru Tunekawa, and Takeshi Hasegawa, Unsteady Flow Past a Circular Cylinder Started Impulsively, Thesis Collection of Japanese Society of Mechanical Engineering, 41, 341 (1975, 1).
3. Madeleine Coutaneeau et Roger Bouard, Sur la Formation de Tourbillons "Secondaires" dans le Sillage d'un Cylindre Soumis à un Départ Impulsif, C. R. Acad. Sc. Paris. T288 (22, Janvier, 1979) Serie B-45.
4. Sarpkaya, T., Separated Flow About Lifting Bodies and Impulsive Flow About Cylinders AIAA. J. 4, 3 (1966).
5. Thoman, D. C., and Szewczyk, A. A., Time Dependent Viscous Flow Over a Circular Cylinder, Physics of Fluids, Suppl. 1969, 12 (II-77-86).
6. Son, J. S., and Hanratty, T. J., Numerical Solution for the Flow Around a Cylinder at Reynolds Number of 40, 200 and 500 J. F. M., 35, part 2 (1969), pp. 369-386.
7. Collins, W. M., and Dennis, S. C. R., Flow Past an Impulsively Started Circular Cylinder, J. F. M., 60, part 1 (1973), pp. 105-127.
8. Patel, V. A., Time Dependent Solution of the Viscous Incompressible Flow Past a Circular Cylinder by Method of Series Truncation, Computers and Fluids, 4 (1976), pp. 13-27.
9. Daffenbaugh, F. D., and Marshall, F. J., Time Development of the Flow About an Impulsively Started Cylinder, AIAA. J., 14, 7 (1976).
10. Ling Guocan, and Yin Xieyuan, Initial-stage Flow of Unsteady Motion of High Reynolds Number Laminar Flow Around a Cylinder, Lixue Xuebao (Acta Mechanica Sinica), Issue No. 2, 1981.
11. Lamb, H., Hydrodynamics, 225-229, Sixth edition, Dover Publications, New York.

NUMERICAL COMPUTATION OF THE VISCOUS COMPRESSIBLE FLOW IN TURBOMACHINERY.  
(II) COMPUTATION OF AXISYMMETRIC FLOW IN THE ROTOR

Jiang Jinliang

Fudan University

Submitted April 1979

The numerical method for computing the viscous compressible steady laminar flow in turbomachinery [1] is applied into rotational coordinate system in this paper. Fundamental equations of the viscous compressible flow in the rotor are introduced. Then, the numerical solution of the viscous axisymmetrical flow in the rotor is obtained by iterative computation based on the enthalpy gradient equation, energy equation and entropy equation, expressed along arbitrary curved lines.

I. Introduction

Since Professor Wu Chunhua proposed a flow surface theory [2], rapid development was made in the calculation method of three dimensional flow in turbomachinery. However, in these calculations the fluid is considered a non-viscous ideal fluid; the mechanical loss caused by fluidity of the fluid can be included by using a loss factor obtained from experiments. Hence the calculation introduces a certain error.

Later, Professor Wu further proposed a viscous flow theory [3] of the turbomachinery flow channel; a detailed analysis was conducted on the physical significance of viscous items. These studies laid a foundation for the numerical calculation of viscous flow in turbomachinery. In recent years, Patankar and Spalding [4] used the progressive integration method to calculate viscous incompressible flow in equal-cross-section straight pipes. Pratap and Majundar [5] used the same method, and calculated viscous incompressible flow of rectangular cross-section straight pipes with flow rotating around the axis perpendicular to the direction of the main stream. However, the calculation of viscous compressible flow problems in the rotor flow channel of turbomachinery did not lead to any solution up to now.

In the first part of paper [1], the author proposed a numerical method of calculating the viscous compressible steady laminar flow problems of an internal flow field. In addition, numerical calculations were conducted on viscous axisymmetric flow\* of a turbomachinery stator. The paper extends this method into a rotating coordinate system, and derives fundamental equations satisfying viscous compressible flow in a rotating coordinate system with rotation around a fixed axis at constant angular velocity. Iterative calculation using these equations can lead to numerical solution of viscous compressible axisymmetric flow in the rotor channel of turbomachinery. This can be approximately considered the numerical solution on the intermediate flow surface  $S_2$ . On this basis, similar methods are used to conduct numerical calculation in the flow surface  $S_1$ . Then the numerical solution of quasi three dimensional flow in the rotor can be obtained.

## II. Fundamental Equations in Rotating Coordinate System

According to the characteristics of streams in turbomachinery, a rotating coordinate system with rotation along the rotor can be established. If it is assumed that the rotating angular velocity of the rotor is constant and the stream in the rotor is an ideal gas, which satisfies Newton's viscosity law and Fourier's law of thermal conduction, then as given in the appendix using the (flow parameters) transformation equation between a stationary coordinate system and rotating coordinate system, it is possible to process the fundamental equations of viscous

\*Refer to paper [1] for mechanical significance of axisymmetric flow.

compressible steady flow in a stationary coordinate system in order to derive fundamental equations satisfying the viscous compressible relative steady flow in the rotating coordinate system:

$$\nabla \cdot (\rho w) = 0 \quad (1)$$

$$(w \cdot \nabla)w + 2\omega \times w + \omega \times (\omega \times R) = F - \frac{1}{\rho} \nabla p + \frac{1}{\rho} \nabla \cdot [\tau] \quad (2)$$

$$w \cdot \nabla h = Q - \frac{1}{\rho} \nabla \cdot q + \frac{1}{\rho} w \cdot \nabla p + \frac{1}{\rho} [\tau] \cdot \nabla w \quad (3)$$

$$p = R\rho T \quad (4)$$

$$h = c_p T \quad (5)$$

In the equations,  $w$  is the relative flow velocity of the stream;  $p$ ,  $\rho$ ,  $T$  and  $h$  are (respectively) the pressure, density, temperature and enthalpy;  $R$  is the gas constant;  $c_p$  is the specific heat at constant pressure,  $F$  is the mass force;  $Q$  is the amount of heat absorption;  $\omega$  is the rotating angular velocity;  $R$  is the position vector of the stream;  $[\tau]$  is the viscous stress tensor; and  $q$  is the amount of heat conduction. These parameters can be expressed as

$$[\tau] = \mu \left\{ \nabla w + (\nabla w)^T - \frac{2}{3} \nabla \cdot w [I] \right\} \quad (6)$$

$$q = -k \nabla T \quad (7)$$

In the equations,  $(\nabla w)^T$  is the transposed tensor of tensor  $(\nabla w)$ ;  $[I]$  is the unit tensor; and  $\mu$  and  $k$  are, respectively, the viscous coefficient and heat conduction coefficient of the fluid. When the temperature varies within a narrow range,  $c_p$ ,  $\mu$  and  $k$  can be approximately considered as constants.

The unknown functions ( $w$ ,  $p$ ,  $\rho$ ,  $T$  and  $h$ ) are included in equations (1) to (5); therefore the equations are closed. Before using this method to conduct numerical calculation, it is necessary to first conduct transformation of the equations by using the similar methods in paper [1]. Also, the transformed fundamental equations in paper [1] can be applied by using the transformed relationship equations of flow parameters in two coordinate systems in the appendix in order to derive the following transformation equations in the rotating coordinate system:

### Flow equation

$$\iint_A \rho \mathbf{w} \cdot d\mathbf{A} = G_0 \quad (8)$$

In the equation,  $A$  is the area of any cross section in the flow channel, and  $G_0$  is the given flow.

### The enthalpy gradient equation

$$\nabla h = T \nabla s + \mathbf{F} + \frac{1}{\rho} \nabla \cdot [\tau] - (\mathbf{w} \cdot \nabla) \mathbf{w} - 2\mathbf{w} \times \mathbf{w} - \mathbf{w} \times (\mathbf{w} \times \mathbf{R}) \quad (9)$$

In the equation,  $s$  is the entropy of the fluid with the equation of entropy as follows:

$$s = R \ln \frac{T^{\frac{K}{K-1}}}{p} \quad (10)$$

In the equation,  $K$  is the adiabatic index of the fluid.

### The energy equation

$$\frac{dI}{dl} = \frac{1}{\mathbf{w}} \left\{ Q + \frac{k}{\rho} \nabla^2 T + \frac{1}{\rho} \nabla \cdot ([\tau] \cdot \mathbf{w}) \right\} \quad (11)$$

In the equation,  $l$  is the spatial streamline;  $d/dl$  is the direction derivative along the streamline  $l$ ;  $I$  is the stagnant transposed enthalpy and its equation is

$$I = h + \frac{\mathbf{w}^2}{2} - \frac{(r\mathbf{w})^2}{2} = h + \frac{\mathbf{v}^2}{2} - r\mathbf{w}\mathbf{v}_0 = h_0 - r\mathbf{w}\mathbf{v}_0 \quad (12)$$

In the equation,  $\mathbf{v}$  is the absolute flow velocity of the stream and  $h_0$  is the stationary enthalpy of the fluid.

### The entropy equation

$$\frac{ds}{dl} = \frac{1}{\mathbf{w}T} \left\{ Q + \frac{k}{\rho} \nabla^2 T + \frac{1}{\rho} [\tau] \cdot \nabla \mathbf{w} \right\} \quad (13)$$

Then, the transformed equations are composed of equations (4), (5), and (8) to (13). In these equations, equation (9) along the streamline direction can be used to derive energy equation (11). Therefore, only two directions can be applied in equation (9). In the equations, the unknown functions included are  $\mathbf{w}$ ,  $p$ ,  $\rho$ ,  $T$ ,  $h$ ,  $s$  and  $I$ ; therefore, the equations are closed and can be used to conduct numerical calculation.

### III. The Boundary Conditions of Equation Forms in Turbomachinery

In turbomachinery, generally the mass force  $F$  and heat absorption  $Q$  are not considered. However, in the axial symmetric flow discussed in the paper, the partial derivative to  $\theta$  of all flow parameters is 0. Then, the above-mentioned equations can be written in the form of a cylindrical-surface coordinate system.

#### The enthalpy gradient equation

For any spatial curve  $q$  in a flow field, the directional derivative of enthalpy  $h$  along the direction of curve  $q$  is

$$\frac{dh}{dq} = T \frac{ds}{dq} + \mathbf{q}^0 \cdot \left\{ \frac{1}{\rho} \nabla \cdot [\mathbf{v}] - (\mathbf{w} \cdot \nabla) \mathbf{w} - 2\mathbf{w} \times \mathbf{w} - \mathbf{w} \times (\mathbf{w} \times \mathbf{R}) \right\} \quad (14)$$

In the equation,  $\mathbf{q}^0$  is the unit vector along the direction of curve  $q$ . Here,  $q$  can be assumed as three directions not on the same plane, thus deriving an equation satisfying the three directions. First, a direction of streamline  $\ell$  is applied; the equation along this direction was used to derive energy equation (11). The  $\theta$  direction is taken as the second direction; for the axisymmetric flow discussed in the paper, this equation does not need to be discussed. The third direction is the direction of the station line [1] approximately perpendicular to the direction of either stream  $\ell$  or  $\theta$ . Then, the enthalpy gradient equation along the station line can be written as

$$\begin{aligned} \frac{dh}{dn} = T \frac{ds}{dn} + & \left\{ \frac{\mu}{\rho} \left[ \frac{4}{3} \left( \frac{\partial^2 w_r}{\partial r^2} + \frac{1}{r} \frac{\partial w_r}{\partial r} - \frac{w_r}{r^2} \right) + \frac{\partial^2 w_r}{\partial x^2} + \frac{1}{3} \frac{\partial^2 w_r}{\partial r \partial x} \right] \right. \\ & - \left. \left[ w_m \frac{dw_r}{dm} - \frac{(w_r + rw)^2}{r} \right] \right\} \frac{dr}{dn} + \left\{ \frac{\mu}{\rho} \left[ \frac{\partial^2 w_r}{\partial r^2} + \frac{1}{r} \frac{\partial w_r}{\partial r} \right. \right. \\ & + \frac{1}{3} \left( 4 \frac{\partial^2 w_r}{\partial x^2} + \frac{\partial^2 w_r}{\partial r \partial x} + \frac{1}{r} \frac{\partial w_r}{\partial x} \right) \left. \right] - w_m \frac{dw_r}{dm} \left. \right\} \frac{dx}{dn} \\ & + \left\{ \frac{\mu r}{\rho} \left[ \frac{\partial^2 w_\theta}{\partial r^2} + \frac{1}{r} \frac{\partial w_\theta}{\partial r} + \frac{\partial^2 w_\theta}{\partial x^2} - \frac{w_\theta}{r^2} \right] \right. \\ & \left. - w_m \frac{d[r(w_\theta + rw)]}{dm} \right\} \frac{d\theta}{dn} \end{aligned} \quad (15)$$

In the equation,  $n$  indicates the projection of the station line on the meridian plane; this is the meridian station line.  $d/dn$  indicates the total derivative of flow parameters varying along the spatial station line to the meridian station line  $n$ .  $d/dm$  indicates the total derivative of the meridian streamline  $m$  of flow parameters varying along the spatial streamline.  $w_r$ ,  $w_\theta$ , and  $w_z$  are components of the relative velocity  $w$  in the cylindrical-surface coordinate system ( $r$ ,  $\theta$  and  $z$ );  $w_n$  is the projection of  $w$  on the meridian plane. Among them, the following equations are satisfied.

$$\left. \begin{aligned} w_r &= w_n \sin \alpha, & w_\theta &= w_n \cos \alpha, \\ w_\theta &= w \sin \beta, & w_n &= w \cos \beta, \end{aligned} \right\} \quad (16)$$

In the equation,  $\alpha$  is the meridian flow angle and  $\beta$  is the circumferential-direction flow angle (Refer to Fig. 1).

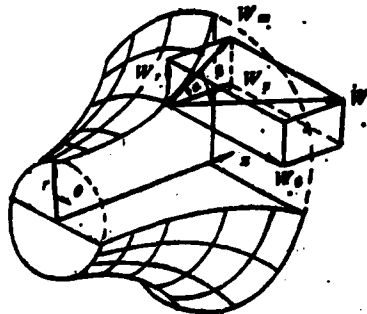


Fig. 1.

For simplicity in calculation, generally the meridian station line  $n$  can be taken as a straight line; this is the quasi-perpendicularly intersecting line as it is usually called. For axial-flow turbomachinery, the meridian station line  $n$  can be more simply applied as the diametral-direction station line. At that time,  $(dz/dn)=0$  in equation (15), which can be simplified into

$$\begin{aligned} \frac{dh}{dr} = T \frac{ds}{dr} + \left\{ \frac{\mu}{\rho} \left[ \frac{4}{3} \left( \frac{\partial^2 w_r}{\partial r^2} + \frac{1}{r} \frac{\partial w_r}{\partial r} \right. \right. \right. \\ \left. \left. \left. - \frac{w_r}{r^2} \right) + \frac{\partial^2 w_r}{\partial s^2} + \frac{1}{3} \frac{\partial^2 w_n}{\partial r \partial s} \right] \right. \\ \left. - \left[ w_n \frac{dw_r}{dm} - \frac{(w_\theta + r\omega)^2}{r} \right] \right\} + \left\{ \frac{\mu r}{\rho} \left[ \frac{\partial^2 w_\theta}{\partial r^2} + \frac{1}{r} \frac{\partial w_\theta}{\partial r} \right. \right. \\ \left. \left. + \frac{\partial^2 w_\theta}{\partial s^2} - \frac{w_\theta}{r^2} \right] - w_n \frac{d[r(w_\theta + r\omega)]}{dm} \right\} \frac{d\theta}{dr} \quad (15') \end{aligned}$$

In the equation,  $d/dr$  is the total derivative of diametral direction  $r$  of flow parameters varying along the spatial station line.

## The energy equation

$$\begin{aligned}
 \frac{dI}{dm} = & \frac{1}{w_m} \left\{ \frac{k}{\rho} \left( \frac{\partial^2 T}{\partial r^2} + \frac{1}{r} \frac{\partial T}{\partial r} + \frac{\partial^2 T}{\partial z^2} \right) \right. \\
 & + \frac{\mu}{\rho} \left[ w_r \left( \frac{4}{3} \frac{\partial^2 w_r}{\partial r^2} + \frac{4}{3r} \frac{\partial w_r}{\partial r} - \frac{4}{3} \frac{w_r}{r^2} + \frac{\partial^2 w_r}{\partial z^2} + \frac{1}{3} \frac{\partial^2 w_r}{\partial r \partial z} \right) \right. \\
 & + w_\theta \left( \frac{\partial^2 w_\theta}{\partial r^2} + \frac{1}{r} \frac{\partial w_\theta}{\partial r} - \frac{w_\theta}{r^2} + \frac{\partial^2 w_\theta}{\partial z^2} \right) + w_z \left( \frac{\partial^2 w_z}{\partial r^2} + \frac{1}{r} \frac{\partial w_z}{\partial r} \right. \\
 & \left. \left. + \frac{4}{3} \frac{\partial^2 w_z}{\partial z^2} + \frac{1}{3r} \frac{\partial w_z}{\partial z} + \frac{1}{3} \frac{\partial^2 w_z}{\partial r \partial z} \right) + 2 \left( \frac{\partial w_r}{\partial r} \right)^2 + 2 \left( \frac{w_r}{r} \right)^2 \right. \\
 & \left. + 2 \left( \frac{\partial w_z}{\partial z} \right)^2 + \left( \frac{\partial w_\theta}{\partial r} - \frac{w_\theta}{r} \right)^2 + \left( \frac{\partial w_\theta}{\partial z} \right)^2 + \left( \frac{\partial w_r}{\partial z} + \frac{\partial w_z}{\partial r} \right)^2 \right. \\
 & \left. \left. - \frac{2}{3} \left( \frac{\partial w_r}{\partial r} + \frac{w_r}{r} + \frac{\partial w_z}{\partial z} \right)^2 \right] \right\} \quad (17)
 \end{aligned}$$

### The entropy equation

$$\frac{ds}{dm} = \frac{1}{w_m T} \left\{ \frac{k}{\rho} \left( \frac{\partial^2 T}{\partial r^2} + \frac{1}{r} \frac{\partial T}{\partial r} + \frac{\partial^2 T}{\partial x^2} \right) + \frac{\mu}{r} \left[ 2 \left( \frac{\partial w_r}{\partial r} \right)^2 + 2 \left( \frac{w_r}{r} \right)^2 + 2 \left( \frac{\partial w_x}{\partial x} \right)^2 + \left( \frac{\partial w_x}{\partial r} - \frac{w_r}{r} \right)^2 + \left( \frac{\partial w_x}{\partial x} \right)^2 + \left( \frac{\partial w_r}{\partial x} + \frac{\partial w_x}{\partial r} \right)^2 - \frac{2}{3} \left( \frac{\partial w_r}{\partial r} + \frac{w_r}{r} + \frac{\partial w_x}{\partial x} \right)^2 \right] \right\} \quad (18)$$

All the three above-mentioned equations are written in derivative form along the non-perpendicularly-intersected curve directions  $m$  and  $n$ . In explicit iterative calculation, these equations are simple differential equations. Numerical calculation can be conducted through numerical integration.

For numerical calculation of viscous compressible axisymmetric flow in a turbomachinery rotor, it is necessary to apply the following boundary conditions:

1. On the internal and external wall surfaces in the rotor flow channel, the relative velocity should be 0; in other words,  $w_{wall}=0$ . The temperature on the wall surface can be given in two ways: (1) with the temperature distribution on the wall surface given, and (2) treated as an adiabatic wall surface, that is the normal-direction derivative of the temperature on the wall surface is 0. According to the relationship between temperature and entropy satisfying equation (5), the boundary conditions of enthalpy on the wall surface can be correspondingly written.
2. When calculating the rotor flow, in order to eliminate the error of arbitrarily selected boundary conditions at inlet and outlet, it is necessary to extend a distance toward the upper and lower streams. As there is no function of blade force in the extension region, in equation (14)  $q$  can be taken as  $\theta$ , and from  $(\alpha h / \alpha \theta) = 0$ , we derive

$$\frac{d[r(w_\theta + rw)]}{dr} = \frac{\mu_r}{\rho w_\theta} \left[ \frac{\partial^2 w_\theta}{\partial r^2} + \frac{1}{r} \frac{\partial w_\theta}{\partial r} + \frac{\partial^2 w_\theta}{\partial x^2} - \frac{w_\theta}{r^2} \right] \quad (19)$$

From the above equation, the distribution of  $w_\theta$  in the extension region can be calculated. On the wall surface is the extension region,  $w_\theta$  can be given in two ways: (1) if the wall surface of the extension region rotates along with the rotor, it can be derived that  $w_\theta|_{wall}=0$ . (2) If the wall surface of the extension region remains stationary, it can be given that  $w_\theta|_{wall}=-rw$ .

#### IV. Numerical Calculation Method and Calculation Examples

This paper adopts the iterative substitution method of the streamline for numerical calculation; the calculation steps are basically the same as the calculation steps mentioned in paper [1]; some slight differences exist in some local calculations. The calculation steps of axisymmetric flow of a rotor are briefly described as follows:

1. On the intermediate flow surface  $S_2$  (including the inner region of the rotor and the extension region toward the upper and lower streams), several station lines  $q$  are selected. According to certain distribution principle of flow, the

assumed streamline  $\ell$  is marked. The streamlines and station lines compose the calculation network; on network points, the distribution situation of  $v_m$ ,  $\rho$  and  $T$  are assumed.

2. The calculation network is projected onto the meridian plane to obtain a meridian network composed of meridian streamline  $m$  and meridian station line  $n$ . By using numerical differentiation, the meridian flow angle  $\alpha$  and meridian station line angle  $\varphi = \arctg \frac{dx}{dr} \Big|$  along  $n$  are obtained.

3. By using an arc shape of the blade, we calculate  $w_\theta = w_m r \frac{d\theta}{dm} \Big|$  along streamline  $\ell$ . For boundary condition (19), iterative calculation is conducted to obtain  $w_\theta$  in the extension region of the upper and lower streams. To reverse the problem,  $w_\theta$  can be calculated according to the selected flow type. Then, we obtain the circumference-direction flow angle  $\beta = \arctg \frac{w_\theta}{w_m}$ .

4. By using direction derivative equations (23) and (24) in paper [1], the partial derivatives of the velocity component and temperatures of  $r$  and  $z$  can be calculated.

5. On each streamline (except the wall surface), we conduct numerical integration for energy equation (17) and entropy equation (18) to obtain distributions of stagnant, transposed enthalpy and entropy in the flow field.

6. On each station line, we conduct numerical integration of the enthalpy gradient equation (15). In addition, by using the boundary condition of the wall surface, the distribution of enthalpy  $h$  can be obtained. Then by using equations (12), (5), (10) and (4), the values of  $w$ ,  $T$ ,  $p$  and  $\rho$  can be obtained. Then by using the flow equation (8), the numerical integration constant can be determined.

7. According to the pre-determined flow distribution principle, new streamline positions can be obtained by reverse calculation. Then, we return to step 2 to conduct the iterative calculation of the next cycle until the required accuracy is satisfied. At that time, the calculation result is the required numerical solution.

By using this method, numerical calculations were conducted on viscous compressible (stationary axis) symmetric flow of a rotor flow channel of an axial-flow-type turbine and compressor. In addition, a comparison is made between the calculation result and experimental result [7] of a TASK-1 stage axial-flow compressor when the relative Mach number is less than 1. Part of calculation results are plotted in Fig. 3. From the figure, it can be seen that the calculation result and experimental result basically match.

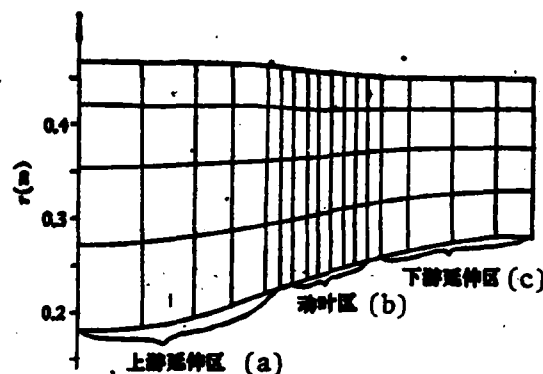


Fig. 2. Distribution diagram of part of meridian streamlines and meridian station lines.

Key: (a) Extension region toward the upper stream; (b) Rotor region; (c) Extension region toward the lower stream.

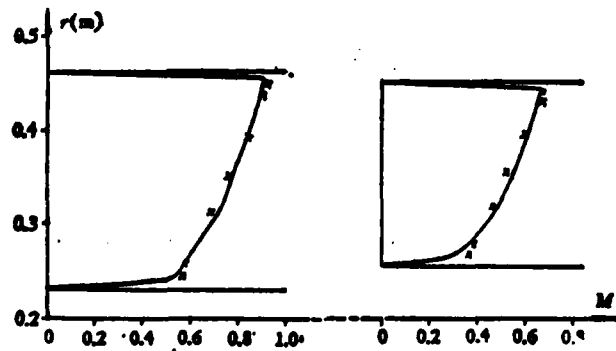


Fig. 3. Relative flow Mach numbers at inlet and exit of rotor: — calculation result; x experimental data.

The characteristics of this method are simple and brief in principle, with fast calculation speed, and not too much computer internal storage required. Hence, this method can be extensively applied to engineering design.

Appendix: Transformation Equations Between the Stationary and Rotating Coordinate Systems of Flow Parameters of a Fluid

For a rotating coordinate system established in the paper, the following relationships exist between the stationary and rotating coordinate systems of flow parameters.

1. The parameters of the flow state do not rely on the selected coordinate system. The total derivative of time and the partial derivatives of various coordinates also do not rely on the selected coordinate system, that is

$$\frac{df}{dt} = \frac{d'f}{ds} \quad (\text{Appendix 1})$$

$$\frac{\partial f}{\partial r} = \frac{\partial' f}{\partial r}, \frac{\partial f}{\partial \theta} = \frac{\partial' f}{\partial \theta}, \frac{\partial f}{\partial s} = \frac{\partial' f}{\partial s} \quad (\text{Appendix 2})$$

In the equations,  $f$  is the parameter of a certain state. The apostrophe at the upper right corner of the differential symbol indicates that the derivation process is conducted in the rotating coordinate system. Otherwise, the derivation process is conducted in the stationary coordinate system. In other parts of the paper, as all discussions are conducted in the rotating coordinate system, this apostrophe is omitted.

2. In a flow field, an arbitrary vector  $\alpha$  (for example, the position vector  $R$  of the mass point of the fluid) does not depend on the selected coordinate system. The total derivatives of time are different in two types of coordinate systems, that is

$$\frac{da}{dt} = \frac{d'a}{ds} + \omega \times a. \quad (\text{Appendix 3})$$

If  $\alpha$  is substituted by  $R$ , the above equation can be written as

$$\frac{dR}{dt} = \frac{d'R}{ds} + \omega \times R,$$

that is,

$$\omega = \omega + \omega \times R \quad (\text{Appendix 4})$$

Or, it is written in component form

$$v_r = \omega_r, v_\theta = \omega_\theta + r\omega, v_s = \omega_s \quad (\text{Appendix 4'})$$

3. By using equations (appendix 3) and (appendix 4), the relationship between the absolute acceleration  $dv/dt$  and the relative acceleration  $d'w/dt$  in the rotating coordinate system can be derived:

$$\begin{aligned}\frac{dw}{dt} &= \frac{d'w}{dt} + \omega \times \omega \\ &= \frac{d'w}{dt} + 2\omega \times \omega + \omega \times (\omega \times \omega)\end{aligned}\quad (\text{Appendix 5})$$

4. According to the above-mentioned equations, the gradients, divergences, degrees of rotation, and Laplace calculation symbols of an arbitrary scalar-quantity field  $\phi$  or vector field  $a$  in the flow field can be derived. (None of these parameters rely on the selected coordinate system.) That is,

$$\nabla \phi = \nabla' \phi, \nabla \cdot a = \nabla' \cdot a, \nabla \times a = \nabla' \times a, \nabla^2 \phi = \nabla'^2 \phi \quad (\text{Appendix 6})$$

5. By using the above-mentioned results, the following results can also be derived:

$$\begin{aligned}\nabla \cdot \omega &= \nabla' \cdot \omega, \quad \nabla \omega = \nabla' \omega, \\ \nabla \cdot [\tau] &= \nabla' \cdot [\tau'], \quad [\tau] \cdot \nabla \omega = [\tau'] \cdot \nabla' \omega\end{aligned}\quad (\text{Appendix 7})$$

In the equations, refer to paper [1] for expression  $[\tau]$ ; refer to equation (6) in the paper for expression  $[\tau']$ .

#### LITERATURE

1. Jiang Jinliang, Numerical Calculation of Viscous Compressible Flow in Turbomachinery Flow Channel. (I) Calculation of Axisymmetric Flow in a Stator, LIXUE XUEBAO [ACTA MECHANICA SINICA], 2 (1981).
2. Wu Chunghua, A General Theory of Three-Dimensional Flow in Subsonic and Supersonic Turbomachines of Axial, Radial and Mixed-Flow Types, NACA TN 2604, 1952.
3. Wu Chunghua, Fundamental Equations of Aerodynamic Thermodynamics in Stationary and Dynamic Coordinate Systems -- Action of Viscous Force and Physical Significance of Viscous Items, JIXIE GONGCHENG XUEBAO [JOURNAL OF MECHANICAL ENGINEERING], 13, 4 (1965).
4. Patankar, S. V., and Spalding, D. B., A Calculation Procedure for Heat, Mass and Momentum Transfer in Three-Dimensional Parabolic Flows, INTERNATIONAL JOURNAL OF HEAT AND MASS TRANSFER, 15 (1972).
5. Pratap, V. S., Majunder, A. K., and Spalding, D. B., Numerical Computation of Flow in Rotating Ducts, T. ASME. SI., 99, 1 (1977).

6. Jiang Jinliang, Streamline Iterative Substitution Method of Calculating Two-Dimensional Viscous Flow, SHANGHAI LIXUE [SHANGHAI MECHANICS], 2, 1 (1981).

7. Koch, C. C., Bilwakesh, K. R., and Doyle, V. L., Evaluation of Range and Distortion Tolerance for High Mach Number Transonic Free Stages, NASA CR-72806, I, II (1971).

PARTIAL DIFFERENTIAL EQUATIONS SATISFIED BY STREAM FUNCTIONS IN THREE DIMENSIONAL TURBOMACHINERY FLOW AND THE FINITE ELEMENT SOLUTION

Li Kaitai, and Huang Aixiang

Jiaotong University, Xi'an

Submitted September 1980

By applying a semi-geodesic coordinate system and tensor analysis, this paper deduces partial differential equations satisfied by stream functions on any stream surface of turbomachinery flow. The paper has also defined a weak problem associated with the boundary value problem for a quasilinear elliptic partial differential equation, and has provided an algorithm of a finite element solution. Two examples are calculated. The establishment of this partial differential equation has brought about a unified method to find the flow solution on any stream surface. Therefore a unified program can be established to realize alternative iteration between  $S_1$  and  $S_2$  on the basis of Wu's theory.

I. Flow Surface and Its Measured Tensor, as Well as Single-Parameter Stream-Surface Family Covering Three-Dimensional Flow Field

We assume any coordinate system  $(x^i)$  in the three-dimensional Euclidean space  $R^3$ . If the parameter equation of a two-dimensional curved surface  $S$  is

$$x^i = x^i(u^a) \quad i = 1, 2, 3$$

In the equation,  $u^a$  ( $a=1, 2$ ) is the Gaussian coordinate system of  $S$ . Then the measured tensor  $g_{ij}$  of  $R^3$  below ( $x^i$ ) and the measured tensor  $a_{\alpha\beta}$  of curved surface  $S$  have the following relationship:

$$a_{\alpha\beta} = g_{ij} \frac{\partial x^i}{\partial u^\alpha} \cdot \frac{\partial x^j}{\partial u^\beta} \quad (1.1)$$

The reverse variation component is  $a^{\alpha\beta} a_{\beta\gamma} = g_{\gamma}^{\alpha}$

That is,

$$a^{11} = a_{xx}/a, \quad a^{12} = a^2 = -a_{xy}/a, \quad a^{21} = a_{yx}/a \quad (1.2)$$

In the equations,  $a = |a_{\alpha\beta}|$  is the matrix of the measured tensor.

For a three-dimensional flow field inside the turbomachinery, we assume the cylindrical coordinate system  $y^1 = r$ ,  $y^2 = \phi$ , and  $y^3 = z$  rotating with the turbine. At that time, the measured tensor is

$$[g_{ij}] = \begin{bmatrix} 1 & 0 & 0 \\ 0 & r^2 & 0 \\ 0 & 0 & 1 \end{bmatrix} \quad (1.3)$$

If there is a flow surface of internal flow in a turbomachinery flow channel, the parameter equation is

$$y^i = y^i(u^\alpha) \quad (1.4)$$

Then the measured tensor of the flow surface is

$$a_{\alpha\beta} = g_{ij} \frac{\partial y^i}{\partial u^\alpha} \frac{\partial y^j}{\partial u^\beta} = \frac{\partial r}{\partial u^\alpha} \frac{\partial r}{\partial u^\beta} + r^2 \frac{\partial \phi}{\partial u^\alpha} \frac{\partial \phi}{\partial u^\beta} + \frac{\partial z}{\partial u^\alpha} \frac{\partial z}{\partial u^\beta} \quad (1.5)$$

The flow surface can be considered formed with a certain rule. Through an arbitrary point, the streamline

$$Y_0 = (y_0^1 = r_0, y_0^2 = \phi_0, y_0^3 = z_0)$$

is the integration curve of the following initial-value problem

$$\left. \begin{array}{l} \frac{dy^i}{ds} = f^i(u^\alpha) \\ y^i|_{s=0} = y_0^i \end{array} \right\} \quad (1.6)$$

In the equation,  $s$  is the arc length of the streamline. However,

$$f = W_r/W, \rho = W_\phi/W/r, \theta = W_z/W$$

$W$  is the relative flow velocity of the stream;  $W = |W|$ ,  $W_r$ ,  $W_\phi$ , and  $W_z$  are physical components of  $W$  in the relative cylindrical coordinate system. The solution of equation (1.6) can be expressed as

$$y^i = y^i(s; Y_0) \quad (1.7)$$

We assume that  $Y_0$  varies on the certain curve  $\ell_0$ ,

$$Y_0 = Y_0(\tau) \quad \tau_0 < \tau < \tau_1 \quad (1.8)$$

Then equation (1.7) can be expressed as

$$y^i = y^i(s; Y_0(\tau)) = g^i(s, \tau) \quad (1.9)$$

It is easy to prove that in case no characteristic direction exists on  $\ell_0$ , the order number of the Jacobi matrix of equation (1.9)

$$J = \begin{bmatrix} \frac{\partial g^i}{\partial s} & \frac{\partial g^i}{\partial \tau} & \frac{\partial g^i}{\partial \tau} \\ \frac{\partial g^i}{\partial s} & \frac{\partial g^i}{\partial \tau} & \frac{\partial g^i}{\partial \tau} \end{bmatrix} \quad (1.10)$$

is 2. Hence, the streamlines passing through any point of  $\ell_0$  compose a curved surface  $S$ ; this is the curved surface. In addition,  $s = u^1$  and  $\tau = u^2$  can be considered the Gaussian coordinate system of the flow surface. Equation (1.9) is the parameter equation of the flow surface with the measured tensor  $a_{\alpha\beta}$ . After substituting equations (1.9) and (1.6) into equation (1.5), we derive

$$\left. \begin{aligned} e_{11} &= g_{11}^{ij} f^j \\ e_{12} &= e_{21} = g_{11}^{ij} \frac{\partial f^j}{\partial \tau} = g_{11}^{ij} \varphi_k \frac{\partial y_k^j}{\partial \tau} \\ e_{22} &= g_{22}^{ij} \frac{\partial f^i}{\partial \tau} = g_{11}^{ij} \varphi_k \varphi_l \frac{\partial y_k^i}{\partial \tau} \frac{\partial y_l^j}{\partial \tau} \end{aligned} \right\} \quad (1.11)$$

In the equations, the matrix  $\{\varphi_k\} = \left[ \frac{\partial y_k^i}{\partial y_0^j} \right]$  is the solution of the variation equation (1.6)

$$\left. \begin{aligned} \frac{d\varphi_k}{ds} &= f^i(s, y) \varphi_k \\ \varphi_k|_{s=0} &= \delta_k^i \end{aligned} \right\} \quad (1.12)$$

$\delta^i_j = \partial f^i / \partial y^j$  and  $\delta^i_k$  are the Kronecker signs.

When  $\iota_0$  moves with certain forms:  $\iota_0 = \iota_0(s)$ ,  $s_0 \leq s \leq s_1$ . Only without appearance of the characteristic direction at an arbitrary position  $s \in [s_0, s_1]$  in the motion process, there is no emergence of a characteristic direction on  $\iota_0$ . Then the integration flow passing through  $\iota_0$  (1.6) forms a single-parameter flow surface family  $S(t)$ , whose Riemann structure is given in equation (1.11). In addition,  $\{S(s) | s \in [s_0, s_1]\}$  covers the entire three-dimensional flow field.

For example, for inlet flows without rotation, a series of arc sectors from blade root to tip (at the turbine inlet) can be selected as  $\iota_0$

$$\left. \begin{array}{l} y_1^i = r_0 = \text{const} \\ y_2^i = \varphi_0, \varphi_1 \leq \varphi_0 \leq \varphi_2 \\ y_3^i = z_0 = \text{const} \end{array} \right\} \quad \dots \quad (1.13)$$

At that time  $\tau = \varphi_0$ , but  $\frac{\partial y_1^i}{\partial \tau} = 0$ ,  $\frac{\partial y_2^i}{\partial \tau} = 1$ ,  $\frac{\partial y_3^i}{\partial \tau} = 0$ . Equation (1.11) can be expressed as

$$\left. \begin{array}{l} e_{11} = g_{11} \mu^i \tau^i \\ e_{12} = e_{21} = g_{12} \mu^i \varphi_1^i \\ e_{31} = g_{31} \varphi_1^i \varphi_2^i \end{array} \right\} \quad (1.14)$$

while taking

$$r_0(s) = R_0 + s(R_1 - R_0) \quad 0 \leq s \leq 1$$

Then  $\iota_0(s)$  moves toward the blade height direction. Here,  $R_1$  and  $R_2$  are radii of the rotor cover and rotor at the inlet. When  $t \in [0, 1]$  varies,  $S(t)$  covers the three-dimensional flow field of the entire flow channel.

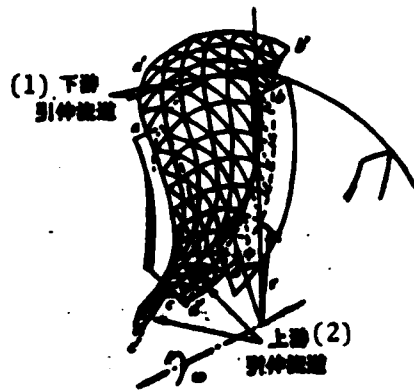


Fig. 1.

Key: (1) Extension flow channel toward the lower stream; (2) Extension flow channel toward the upper stream.

## II. Differential Equations of Flow Functions on Arbitrary Flow Surfaces

We assume that a turbine rotates with angular velocity  $\omega$ ;  $W$  is the relative flow velocity of the fluid;  $T$  is the fluid temperature;  $s$  is entropy;  $I = i + (W^2/2) - (\omega^2 r^2/2)$  is the transposed enthalpy; and  $i$  is the density enthalpy of the fluid. Then the continuous equation and momentum equation of internal flow of the turbomachinery are

$$\nabla \cdot (\rho W) = 0 \quad (2.1)$$

$$W \times (\nabla \times W) - 2\omega \times W = \nabla I - T \nabla s \quad (2.2)$$

In the equations,  $\rho$  is the fluid density.

We introduce the matrix tensor

$$g_{ijk} = \begin{cases} \sqrt{s} & \epsilon^{ijk} = \begin{cases} 1/\sqrt{s} & \text{where } i, j \text{ and } k \text{ are even row of (1,2,3)} \\ -1/\sqrt{s} & \text{where } i, j \text{ and } k \text{ are odd row of (1,2,3)} \\ 0 & \text{for other situations} \end{cases} \end{cases} \quad (2.3)$$

In the matrix,  $g = |g_{ij}|$  is the matrix of the measured tensor.  $\epsilon_{ijk}$  and  $\epsilon^{ijk}$  are asymmetric to any pair of indexes. In addition, there is the accompanying tensor:

$$\epsilon_{ijk} = g_{im} g_{jn} g_{kn} \epsilon^{mnp} \quad (2.4)$$

The degree of rotation and vector product can be expressed as

$$\begin{aligned}\nabla \times W &= \epsilon^{ijk} (\nabla_i w_k - \nabla_k w_i) e_i / 2 \\ \omega \times W &= g^{ik} \epsilon_{mjk} \omega^m w^m e_i\end{aligned}\quad (2.5)$$

In the equations,  $\{e_i\}$  is the covariant fundamental vector of  $\{x^i\}$  coordinate system;  $w_i$  and  $w^i$  are, respectively, the covariant component and reverse variant component of  $W$ ; and  $\nabla_i$  is the covariant derivative of the tensor. Therefore, equation (2.2) can be expressed as

$$\frac{1}{2} g^{ik} \epsilon_{mjk} \epsilon^{m\ell} w^\ell (\nabla_i w_\ell - \nabla_\ell w_i) - 2 g^{ik} \epsilon_{mjk} \omega^m w^m = g^{ik} (\nabla_i I - T \nabla_i S) \quad (2.6)$$

$g^{ik}$  is the reverse variant component of the measured tensor.

First, the semi-geodesic coordinate system  $(x^i)$  of the stream surface  $S$  is considered as the fundamental curved surface; then the following relationships obtain between the measured tensor  $g_{ij}$  of  $R^3$  below  $(x^i)$  and the measured tensor  $a_{\alpha\beta}$  of the stream surface  $S$ :

$$\begin{aligned}g_{00} &= a_{00}, \quad g_{10} = g_{20} = 0, \quad g_{30} = 1, \quad g = a \\ g^{00} &= a^{00}, \quad g^{10} = g^{20} = 0, \quad g^{30} = 1\end{aligned}\quad (2.7)$$

Under the semi-geodesic coordinate system,

$$w^i|_s = w_i|_s = 0 \quad (2.8)$$

We substitute the equations (2.7) and (2.8) into equation (2.6), and we obtain

$$\begin{aligned}\frac{1}{2} a^{r0} \epsilon_{R0s} \epsilon^{R\ell} w^\ell (\nabla_i w_s - \nabla_s w_i) - 2 a^{r0} \epsilon_{R0s} \omega^s w^s \\ = a^{r0} (\nabla_i I - T \nabla_i S)\end{aligned}\quad (2.9)$$

By utilizing  $\epsilon^{ijk}$  and  $\epsilon_{ijk}$  concerning their index asymmetric characteristic, we obtain

$$\begin{aligned}\frac{1}{2} a^{r0} \epsilon_{R0s} \epsilon^{R\ell} w^\ell (\nabla_i w_s - \nabla_s w_i) \\ = a^{r0} \epsilon_{R0s} w^\ell \epsilon^{R\ell} (\nabla_i w_s - \nabla_s w_i) \\ = (a^{r1} w^2 - a^{r2} w^1) (\nabla_i w_s - \nabla_s w_i)\end{aligned}$$

From equation (1.2) and  $w_s = a_{s0} w^0$ , equation (2.9) can be expressed as

$$\begin{aligned}w_2 [(\nabla_i w_2 - \nabla_2 w_i) + 2 \sqrt{-a} \omega^3] &= a a^{10} (\nabla_i I - T \nabla_i S) \\ w_1 [(\nabla_i w_2 - \nabla_2 w_i) + 2 \sqrt{-a} \omega^3] &= -a a^{20} (\nabla_i I - T \nabla_i S)\end{aligned}$$

or

$$\nabla_1 w_2 - \nabla_2 w_1 + 2\sqrt{\sigma} \omega^3 = f \quad (2.10)$$

$$f = \begin{cases} \sigma \omega^3 (\nabla_0 I - T \nabla_0 \omega) / w_2 & \text{when } w_2 \neq 0 \\ -\sigma \omega^3 (\nabla_0 I - T \nabla_0 \omega) / w_1 & \text{when } w_1 \neq 0 \end{cases} \quad (2.11)$$

Under the semi-geodesic coordinate system, the normal direction of the stream surface is  $n$ , which is consistent with  $e_3$ :

$$n = e_3 = \sigma^1, n \cdot e_0 = 0 \quad (2.12)$$

Then, from equation (2.5) we obtain

$$n \cdot \text{rot} W = (\nabla_1 w_2 - \nabla_2 w_1) / \sqrt{\sigma} \quad (2.13)$$

Substituting into equation (2.10), we obtain

$$n \cdot \text{rot} W + 2n \cdot \omega = f / \sqrt{\sigma} \quad (2.14)$$

This is the equation of the degree of rotation on the stream surface.

Equation (2.1) can be expressed as

$$\frac{\partial}{\partial x^a} (\sqrt{\sigma} \rho \omega^a) + \frac{\partial}{\partial x^b} (\sqrt{\sigma} \rho \omega^b) = 0$$

By noting equation (2.8), on the stream surface there is

$$\frac{\partial}{\partial x^a} (\sqrt{\sigma} \rho \omega^a) + \rho \sqrt{\sigma} \frac{\partial \omega^a}{\partial x^a} = 0 \quad (2.15)$$

We assume  $b(x^a)$  satisfies an one-order partial differential equation:

$$\omega^a \frac{\partial \ln b}{\partial x^a} \Big|_s = - \frac{\partial \omega^a}{\partial x^a} \Big|_s \quad (2.16)$$

Then, we obtain a continuous equation (on the stream surface)

$$\frac{\partial}{\partial x^a} (b \sqrt{\sigma} \rho \omega^a) = 0 \quad (2.17)$$

In the equation,  $b(x^a)$  is an arbitrary integration of equation (2.16). It can be proved that the mechanical significance is the relative thickness of the stream slice.

By introducing flow function  $\psi(x^a)$  satisfying

$$\left. \begin{array}{l} \frac{\partial \psi}{\partial x^1} = -b\rho \sqrt{\sigma} w^2 \\ \frac{\partial \psi}{\partial x^2} = b\rho \sqrt{\sigma} w^1 \end{array} \right\} \quad (2.18)$$

If  $\psi$  exists, then  $w^\alpha$  determined by equation (2.18) can automatically satisfy the continuity equation (2.17).

By substituting equation (2.18) into equation (2.10), we obtain the equation (of  $\psi(x^\alpha)$ )

$$-\frac{\partial}{\partial x^\alpha} \left( \frac{\sqrt{\sigma}}{b\rho} a^{\alpha\beta} \frac{\partial \psi}{\partial x^\beta} \right) + F = 0 \quad (2.19)$$

In the equation,  $F = 2\sqrt{\sigma} w^3 - f$ . When the stream surface is the real Riemann curved surface,  $a^{\alpha\beta}$  is positively symmetric.

The boundary  $\Gamma = \Gamma_0 \cup \Gamma_s \cup \Gamma_p$  of the stream surface is composed of three parts:  $\Gamma_0$  is the inlet-outlet of the flow;  $\Gamma_s$  is the intersecting line of the stream surface and solid wall (blades, rotor, or rotor cover);  $\Gamma_p$  is the artificial boundary line.  $\psi$  should satisfy

$$\left. \begin{array}{l} \frac{\sqrt{\sigma}}{b\rho} a^{\alpha\beta} \psi_{,x^\beta} n_\alpha |_{r_0} = g \\ \psi |_{r_0} = \phi, \\ \psi |_{r_{p1}} = \psi |_{r_{p2}} + G, \quad \left. \frac{\partial \psi}{\partial n} \right|_{r_{p1}} = \left. \frac{\partial \psi}{\partial n} \right|_{r_{p2}} \end{array} \right\} \quad (2.20)$$

In the equation,  $(n_\alpha)$  is the covariant component of the unit vector of the external normal of the boundary.

The physical components  $W_r$ ,  $W_\phi$ , and  $W_z$  (in the cylindrical coordinate system of  $W$ ) can be derived through  $w^\alpha$ , that is

$$W_r = \frac{\partial r}{\partial x^\alpha} w^\alpha, \quad W_\phi = r \frac{\partial \phi}{\partial x^\alpha} w^\alpha, \quad W_z = \frac{\partial z}{\partial x^\alpha} w^\alpha \quad (2.21)$$

By using equation (2.18), it is easy to derive a calculation equation (of flow density)

$$b\rho W = \sqrt{a^{\alpha\beta} \psi_{,x^\alpha} \psi_{,x^\beta}} \quad (2.22)$$

According to the relationship between  $\rho$  and  $W$ , there is

$$\rho = \rho_0 (c - (r - 1) a^{\alpha\beta} \psi_{,x^\alpha} \psi_{,x^\beta} / (2 a^{\alpha\beta} \rho^2))^{1/(r-1)} \quad (2.23)$$

In the equation,  $c = 1 - (\gamma - 1)(\omega^2 r^2 - 2\omega\lambda)/2a_s^2$ ;  $\rho_s$  and  $a_s$  are, respectively, the stagnant density and stagnant sound velocity of the reference point;  $\lambda$  is the degree of pre-rotation.

Hence, equations (2.19) and (2.20) are nonlinear boundary-value problems. When the flow is subsonic, then these are nonlinear elliptical boundary-value problems.

When the parameter equations are determined in the following forms:

$$r = r(x^a), \varphi = \varphi(x^a), z = z(x^a)$$

then

$$\begin{aligned} a_{\alpha\beta} &= r_{,\alpha}r_{,\beta} + r^2\varphi_{,\alpha}\varphi_{,\beta} + z_{,\alpha}z_{,\beta} \\ \omega^3 &= r\omega(r_{,\alpha}\varphi_{,\beta} - r_{,\beta}\varphi_{,\alpha})/\sqrt{a} \end{aligned}$$

If the stream surface is a rotating surface, let  $z=z(m)$  and  $r=r(m)$  be the parameter equations of the generatrix. Then by assuming  $x^1=m$  and  $x^2=\phi$ ,

$$\begin{aligned} a_{11} &= 1, a_{12} = a_{21} = 0, a_{22} = r^2, a = r^2 \\ \omega^3 &= \omega \cdot dr/dm \end{aligned}$$

It is of some importance that the blade surface, rotor and rotor cover in the flow channel are natural stream surfaces. Hence, these stream surface equations are known. In the case of the blade surface, if its parameter equation is  $\phi=\phi(r, z)$ . At that time, by taking  $x^1=z$  and  $x^2=r$ , then

$$\begin{aligned} a_{11} &= 1 + r^2\varphi_z^2, a_{12} = a_{21} = r^2\varphi_r\varphi_z, a_{22} = 1 + r^2\varphi_r^2, \\ a &= 1 + r^2(\varphi_z^2 + \varphi_r^2), \omega^3 = -r\omega\varphi_z/\sqrt{a} \end{aligned}$$

can be directly solved for boundary-value problems (2.19) and (2.20) in order to obtain the distribution of the stream field at the surface of blade. The flow-field distribution at the blade surface is the main basis for determining the aerodynamic characteristics of blade types.

### III. Approaching a Solution of Finite Elements

If  $(x^1, x^2) \in \Omega$  and  $V$  is a Banach space, satisfying  $H_0^1(\Omega) \subset V \subset H^1(\Omega)$ .

$$V = \left\{ u \mid u \in H^1(\Omega), u|_{\Gamma_1} = 0, u|_{\Gamma_2} = u|_{\Gamma_3}, \frac{\partial u}{\partial n} \Big|_{\Gamma_2} = \frac{\partial u}{\partial n} \Big|_{\Gamma_3} \right\}.$$

then corresponding to equations (2.19) and (2.20), the simulated dual-linear arbitrary function (over  $V \times V$ ) is

$$B(\phi, \phi^*) = \iint_{\Omega} \frac{\sqrt{\sigma}}{b\rho} \sigma^{\alpha\beta} \phi_{,\alpha} \phi_{,\beta} dx^1 dx^2 \quad (3.1)$$

and the linear arbitrary function

$$\langle Fg, \phi^* \rangle = \iint_{\Omega} F \phi^* dx^1 dx^2 - \int_{\Gamma_0} g \phi^* dl \quad (3.2)$$

We assume  $\hat{\phi} \in H^1(\Omega)$ , which satisfies  $\hat{\phi}|_{\Gamma_0} = \phi_0$ ,  $\hat{\phi}|_{\Gamma_1} = \hat{\phi}|_{\Gamma_2} + G$ ,  $\frac{\partial \hat{\phi}}{\partial n}|_{\Gamma_1} = \frac{\partial \hat{\phi}}{\partial n}|_{\Gamma_2}$ .

Then, the weak solution of the boundary-value problem of equations (2.19) and (2.20) is: we solve for  $\phi - \hat{\phi} \in V$ , so that

$$B(\phi, \phi^*) = \langle Fg, \phi^* \rangle \quad \forall \phi^* \in V \quad (3.3)$$

We assume that  $V_n \subset V$  is the  $n$ -dimensional subspace and its fundamental function system is  $(\phi_i)_{i=1}^n$ . The Galerkin approach solution of equation (3.3) is expressed as

$$\phi_n = \hat{\phi} + c^i \phi_i \quad (3.4)$$

Then  $(c^i)_{i=1}^n$  should satisfy the algebraic equation

$$A_N(\mathbf{c}) \mathbf{c}^k - \mathbf{F}_N(\mathbf{c}) = 0 \quad (3.5)$$

In the equation

$$A_N(\mathbf{c}) = \iint_{\Omega} \frac{\sqrt{\sigma}}{b\rho} \sigma^{\alpha\beta} \phi_{i,\alpha} \phi_{k,\beta} dx^1 dx^2 \quad (3.6)$$

$$\mathbf{F}_N(\mathbf{c}) = - \iint_{\Omega} \frac{\sqrt{\sigma}}{b\rho} \sigma^{\alpha\beta} \hat{\phi}_{,\alpha} \phi_{i,\beta} dx^1 dx^2 + \int_{\Gamma_0} g \phi_i dl + \iint_{\Omega} f \phi_i dx^1 dx^2 \quad (3.7)$$

It can be proved that the solution of algebraic equation (3.5) exists. Hence, the Galerkin approach solution of equation (3.4) also exists. It can be proved that the solution is also convergent.

#### IV. Calculation Examples

By using the derived differential equations (2.19) and (2.20) for boundary-value problems, solutions are obtained by using the finite-element method to

separately calculate flow fields of a T1102 blade type and Gostelow accurate-solution blade grid. In calculations, the finite-element network used is an arbitrary quadrilateral (on a curved surface); the element types are eight-nodal-point quadrilateral and other parameter elements. Compare the calculation results with that of the T1102 blade type and experimental results as shown in Fig. 2; also compare the results with that of the Gostelow blade grid and theoretical solution as shown in Fig. 3. Both comparisons match to each other relatively well.

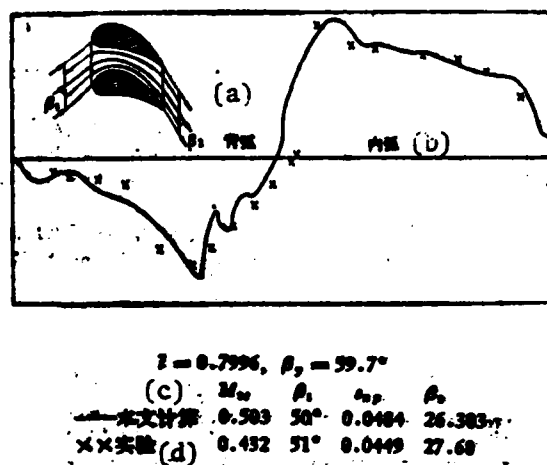


Fig. 2. Comparisons of experimental values with T1102 blade-type plane blade grid in pressure distribution along the blade surface.  
 Key: (a) Back arc; (b) Internal arc; (c) Calculated in the paper; (d) xx experiments.

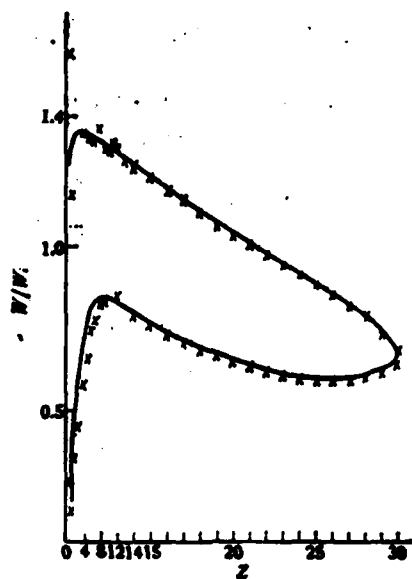


Fig. 3. Comparisons with accurate solution of velocity distribution at blade surface of GOSTELOW blade grid: — accurate solution; x finite-element solution in the paper.

#### LITERATURE

1. Wu Chunghua, Three Dimensional Turbomachine Flow Equations Expressed With Respect to Non-orthogonal Curvilinear Coordinates and Methods of Solution, The Third Int. Symp. on Air Breathing Engines held at Munich 1976.
2. Wu Chunghua, A General Theory of Three Dimensional Flow in Subsonic or Supersonic Turbomachine of Axial Radial and Mixed Flow Types, ASME paper No. 50-A-79, 1950; NACA TN 2604, 1952.
3. Li Kaitai, Solution Determination Problem and Its Finite Element Solution of Differential Equations in Semi-Geodesic Coordinate System of Stream Functions on  $S_1$  and  $S_2$ , Stream Surfaces of Quasi-Three-Dimensional Flow in Turbomachinery, XI'AN JIAOTONG DAXUE XUEBAO [BULLETIN OF JIAOTONG UNIVERSITY, XI'AN], 1 (1978), 31-60.
4. Hirsch, C. H., and Warzee, G., A Finite Elements Method for the Axisymmetric Flow Computation in a Turbomachine, INT. J. NUMER. ENG., 10, 1 (1976), 93-113.
5. Hirsch, C. H., and Warzee, G., A Finite Element Method for Through Flow Calculations in Turbomachines, ASME paper 76-FE-12, 1976.

6. Alder, D., and Krimerman, Y., The Numerical Calculation of the Meridional Flow Field in Turbomachines Using the Finite Elements Method, ISRAEL J. TECH., 12, 3/4 (1974).
7. Alder, D., and Krimerman, Y., Calculation of the Blade to Blade Compressible Flow Field in Turbomachines Using the Finite Element Method, J. MECH. ENG. SCIENCE, 19, 3 (1977).
8. Gelder, D., Solution of the Compressible Flow Equations, INT. J. NUM. METH. ENG., 3 (1971), 35-45.
9. Li Kaitai, and Huang Aixiang, Finite Element Analysis of Electric Field Distribution of Compound-Layer Medium, BULLETIN OF JIAOTONG UNIVERSITY, XI'AN, 3 (1978).
10. Browder, F. E., Problemes Non Lineaires, Les Presses de l' Universite de Montreal (1966).

## IRIDIUM ELECTROSTATIC PROBE AND ITS APPLICATION IN A HIGH TEMPERATURE WIND TUNNEL

Wang Boyi

Institute of Mechanics, Chinese Academy of Sciences

Submitted September 1979

The paper describes a kind of electrostatic probe which can be used to measure parameters of high temperature gas flow for such parameters as electron density and electron temperature. The paper also gives theoretical curves of probe characteristics for air plasma. This iridium electrostatic probe has been operated successfully in an electric-arc-heated wind tunnel.

### I. General Descriptions

In experiments and studies of high temperature high speed aerodynamics, as well as experiments and studies of an aerodynamic laser and electromagnetic fluid dynamics, the electron density and electron temperature of a high temperature medium are very important parameters; these parameters have to be measured experimentally. The paper introduces a type of electrostatic probe applied in measuring electron density and electron temperature of a gas stream in high temperature wind tunnels.

The electrostatic probe is an important tool for plasma diagnostics [1]. The measuring and testing system of the electrostatic probe is simple, with a large dynamic range. The probe can measure the local value of parameters. The so-called electrostatic probe is actually a metallic electrode. The probe is placed in the gas to be measured; the external power source provides voltage to obtain a certain value of the potential relative to the gas to be measured. A certain number of electrons and ions are collected from the gas to form a current. When the potential of the probe varies, the probe current will vary according to a fixed rule. After testing, the "volt-ampere characteristics" of the probe are obtained. The volt-ampere characteristics are related to parameters such as density and temperature of charged particles. The probe theory can give the quantitative relationship between density and temperature of the charged particles in the gas.

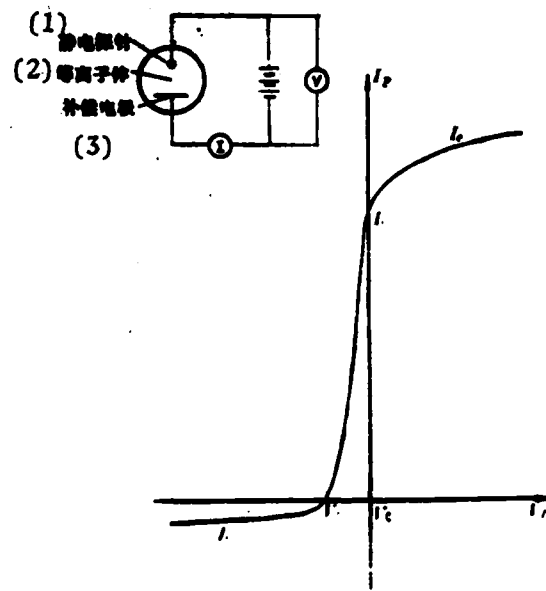


Fig. 1. Electrostatic probe and its volt-ampere characteristic curve.  
Key: (1) Electrostatic probe; (2) Plasma;  
(3) Compensation electrode.

In the severe hot environment of a high temperature wind tunnel, first the problem of survival of the probe in the high temperature stream has to be solved by using an electrostatic probe for measurement. Hence, we developed an iridium electrostatic probe, and it has been successfully operated in the H-4 electric-arc-heated wind tunnel to calibrate electron density and electron temperature of the testing stream and its cross section. Basically, the calibration result agrees with the theoretical calculation.

## II. Structural Design of Iridium Electrostatic Probe

According to the high-temperature and high-speed characteristics of the electric-arc-heated wind tunnel, the electrostatic probe we developed is composed of three parts: central electrode, insulation lining, and water-cooling sleeve.

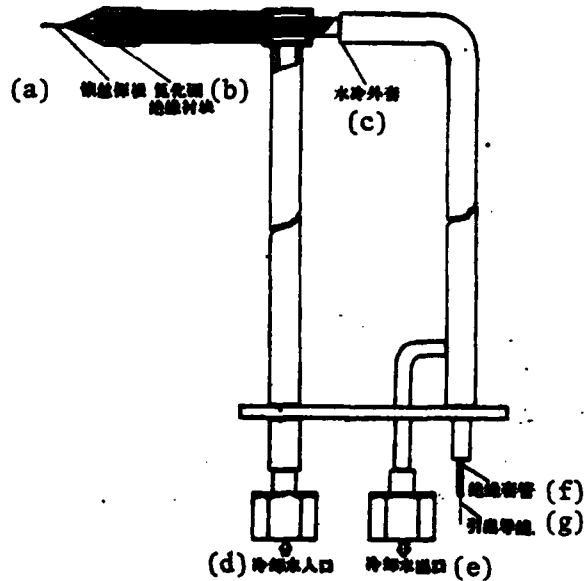


Fig. 2. Structural diagram of iridium electrostatic probe.

Key: (a) Iridium probing electrode; (b) Boron nitride insulation lining; (c) Water-cooling sleeve; (d) Inlet of cooling water; (e) Outlet of cooling water; (f) Insulation sleeve; (g) Lead-out wire.

The central electrode includes the iridium probe, lead-out wire, heat-endurance insulation sleeve, and others. Iridium wire has the advantages of high melting temperature, good electrical and heat conductivities, high energy function, and resistance to oxidation. In addition, the iridium wire is hard and stiff, so it is quite adaptable to be used as probes for operation in a high-temperature air environment. As proved by experiments, this iridium electrostatic probe can be successfully and continuously operated in a gas stream of 14.6 MJ/kg of entropy and 20 g/s of flow.

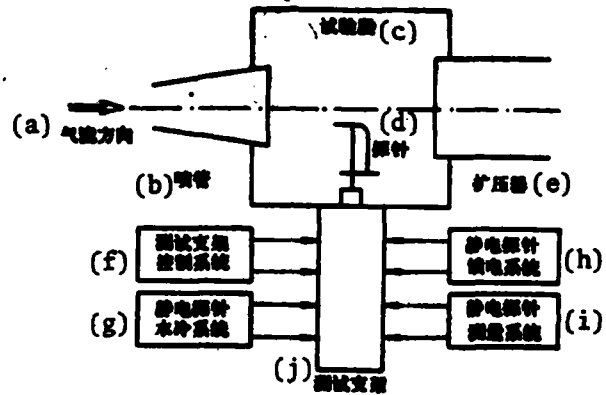


Fig. 3. Schematic diagram of iridium electrostatic probe system for calibration of electric-arc-heated wind tunnel.  
 Key: (a) Direction of gas stream; (b) Nozzle; (c) Testing sector; (d) Probe; (e) Pressure expander; (f) Control system of test stand; (g) Water cooling system of electrostatic probe; (h) Power feed system of electrostatic probe; (i) Measurement system of electrostatic probe.

A high pressure (28 atmospheric pressures) water pump is used in the water-cooling sleeve. Besides providing protection for the central electrode, the sleeve is also used as a compensation electrode of the probe.

The insulation lining can ensure electrical insulation between the external water sleeve and the iridium electrode; boron nitride is used for the lining, as

the material is high in insulation, burn etching and heat conduction characteristics. Therefore, some cooling effect can be provided for the iridium wire by these characteristics. A high-temperature seal is used between the central electrode and boron nitride.

The entire probe is placed on a test stand of a three-dimensional wind tunnel.

### III. Theory and Data Analysis of Electrostatic Probe

The theoretical analysis of the electrostatic probe is relatively complex. In particular, in calibration of the gas stream in a wind tunnel, the flow effect and electrostatic effect of the plasma should be coupled; thus, the theoretical description is even more complex. In order to avoid considering the flow effect, we used a cylindrical probe with its axial line parallel to the direction of the gas stream velocity. In addition, the probe diameter should be sufficiently small in order to satisfy the theoretical requirements of the electrostatic probe of free molecules:

$$D, R_p \ll \lambda$$

In the expression,  $D$  is the length of the Durban screen;  $R_p$  is the probe radius; and  $\lambda$  is the average free range of charged particles in the gas stream.

High temperature gas is a partially ionized plasma; in the plasma the densities of electrons and ions are equal to each other,  $n_e = n_i$  ( $n_e$  and  $n_i$  are, respectively, densities of electrons and ions). Hence, the probe current is composed of electron current and ion current:  $I_p = I_e - I_i$ . In the equation,  $I_p$  is the probe current;  $I_e$  is electron current; and  $I_i$  is ion current. We can see from Fig. 1 that when the probe potential  $V_p$  is lower than the space potential  $V_0$  of the plasma (generally, it is called the negative probe), the probe will attract ions but reject electrons. The higher the negative value of the potential, the more are electrons rejected. Hence, the probe current drops rapidly. At the floating potential  $V_f$ , the electron current and ion current are equal in value and the probe current is zero. When the probe potential is considerably lower

than the floating potential, the probe collects almost all the ion current. Besides, the current varies very slowly with the potential; generally, such a current is called the saturated ion current.

An accurate probe theory [2] gives the expression for the ion current:

$$j_i = e m_i \left( \frac{k T_e}{2 \pi m_i} \right)^{1/2} I_+(x_p, \xi, \epsilon) \quad (1)$$

In the equation,  $j_i$  is the density of the ion current of the probe;  $e$  is the electron charge;  $T_e$  is the electron temperature;  $m_i$  is the ion quality;  $k$  is Boltzmann's constant;  $I_+$  is the current density of dimensionless ions; and  $x_p$ ,  $\xi$  and  $\epsilon$  are dimensionless variables. Their definitions are:

$$x_p = \frac{e V_p}{k T_e}, \quad \xi = \frac{R_p}{D}, \quad \epsilon = \frac{T_i}{T_e}$$

In the equations,  $T_i$  is the ion temperature. In paper [2], a numerical method is used to obtain the dimensionless function  $I_+$  as the calculation results of the functions  $x_p$ ,  $\xi$  and  $\epsilon$ . Starting from this result, we derived theoretical curves (refer to Fig. 4) adaptable to air plasma; the abscissa is  $\xi I_+(x_i - 10)$ ,

and the ordinate is  $I_+(x_i - 10)$ . Here,  $x_i = \frac{e V_i}{k T_e}$ , which is the dimension-

less floating potential.  $I_+(x_f - 10)$  indicates that the potential is lower than the floating potential by a dimensionless value of densities of ions and current at 10( $k T_e / e$ ) volts. When the electron temperature  $T_e$  is known, in the volt-ampere characteristics of the probe measured by experiments, it is not difficult to determine the position of  $(x_f - 10)$ ; the value of  $I_+(x_f - 10)$  can be found accordingly.

Thus, it is required to first determine electron temperature from plotted curves as shown by the two following methods:

1. The inclination of a semi-logarithmic curve of electron current of the negative probe:

$$\frac{k T_e}{e} = \frac{1}{\frac{d}{d V_p} (\ln I_e)} \quad (2)$$

2. The inclination of the probe characteristic curve at the floating potential

$$\frac{kT_e}{e} = \left[ \frac{I_p}{\frac{dI_p}{dV_p}} - \left| \frac{dI_p}{dV_p} \right| \right] \Big|_{V_p = V_f} \quad (3)$$

Electron temperature values can be simply determined by using a graphic method (Fig. 5).

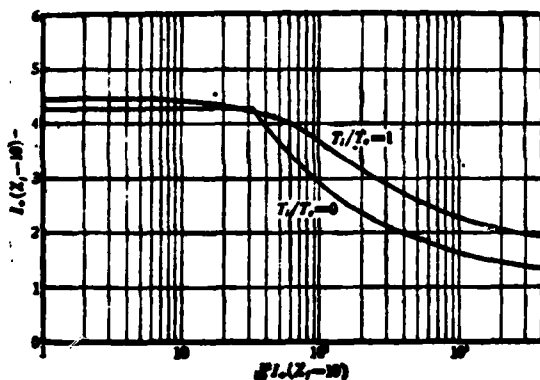


Fig. 4. Electrostatic probe: theoretical curves in air plasma.

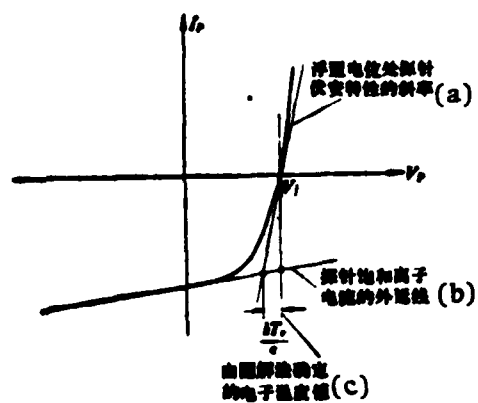


Fig. 5. Graphic method of determining electron temperature.

Key: (a) Inclination of volt-ampere characteristic of probe at floating potential; (b) Extension line of saturated ion current of the probe; (c) Electron temperature value determined by graphic method.

Given a known electron temperature, we can utilize the measured probe characteristics and the given theoretical curves to determine the density of electrons or ions. We use the following steps:

1. From the measured ion-current curve of the probe,  $I_i(x_f-10)$  can be determined.

2. We calculate the density of the ion current at potential  $(x_f-10)$

$$j_i(x_f-10) = \frac{I_i(x_f-10)}{A_p} \quad (4)$$

In the equation,  $A_p = 2\pi R_p l$  is the surface area of the probe;  $l$  is the length of the probe.

3. We calculate the corresponding value of  $\xi^2 I_+(x_f-10)$

$$\xi^2 I_+(x_f-10) = 1.563 \times 10^8 R_p^2 \frac{j_i(x_f-10)}{\left(\frac{kT_e}{e}\right)^{\frac{1}{2}}} \quad (5)$$

In the equation, the unit of  $R_p$  is M; the unit of  $j_i$  is  $A/M^2$ ; and the unit of  $kT_e/e$  is V.

4. From the theoretical curve (Fig. 4) of the probe, the  $I_+(x_f-10)$  value of  $\xi^2 I_+(x_f-10)$  is determined.

5. We calculate the corresponding value of the ion density

$$n_i = \frac{j_i(x_f-10)}{e \left(\frac{kT_e}{2\pi m_i}\right)^{\frac{1}{2}} I_+(x_f-10)} \\ = 8.64 \times 10^{10} \frac{j_i(x_f-10)}{I_+(x_f-10)} \left(\frac{e}{kT_e}\right)^{\frac{1}{2}} \quad (6)$$

In the equation, the unit of  $n_i$  is  $[1/M^3]$ ; other units are the same as above. For plasma,  $n_e = n_i$ ; therefore, the electron density is also determined.

#### IV. Calibration Result of Electron Density in Gas Stream During Wind Tunnel Testing Sector

By using the iridium electrostatic probe, calibration tests were conducted in the H-4 electric-arc-heated wind tunnel. The basic characteristic parameters of the H-4 wind tunnel are as follows:

Electric power source: 1500 kW; Work medium: air; Gas flow: 15-40 g/s; Gas pressure in electric-arc-heated chamber:  $3 \times 10^5$  -  $10^6$  N/m<sup>2</sup>; and total entropy of gas: 8-18 MJ/kg. In addition, the throat diameter of the nozzle is 8.1 mm; the exit diameter is 220 mm; the total pressure in the testing sector during measurement is approximately  $3 \times 10^2$  N/m<sup>2</sup>; and the static pressure is approximately 3 N/m<sup>2</sup>.

According to the operation parameters of the wind tunnel mentioned above, we calculated the theoretical values of the electron density and electron temperature of the test gas stream (during estimation and calculation, the pressure of the electric-arc-heated wind tunnel is assumed to be  $6.87 \times 10^5$  N/m<sup>2</sup>, that is 6.8 atmospheric pressures). Results are shown in Figs. 6 and 7.

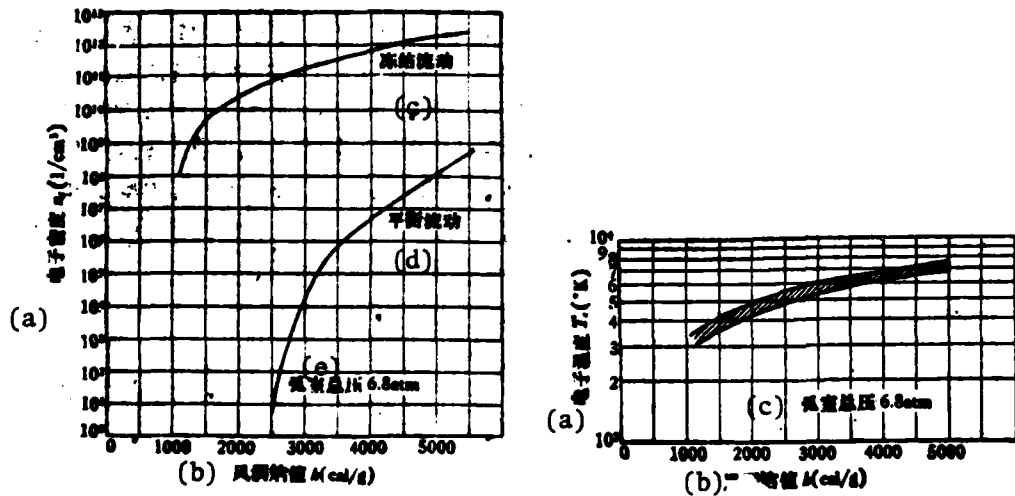


Fig. 6. Estimation-calculation of electron density of test gas stream in H-4 electric-arc-heated wind tunnel.

Key: (a) Electron density; (b) Entropy value of wind tunnel; (c) Frozen flow; (d) Balanced flow; (e) Total atmospheric pressure in the heated chamber. 50

Fig. 7. Estimation-calculation of electron temperature range of test gas stream of H-4 heated chamber.

Key: (a) Electron temperature; (b) Entropy value of wind tunnel; (c) Total atmospheric pressure in electric-arc-heated chamber.

Calibration testing proceeds in two stages. The first stage emphasizes the measurement of local values of parameters such as electron density. At three different cross sections of the gas stream, testing points in all were tested. The entire volt-ampere characteristic is obtained by scanning with a voltage probe. After compilation, typical measurement-testing results are plotted in Figs. 8 and 9. We know from these measurement results that the test gas stream of the H-4 electric-arc-heated wind tunnel approaches a frozen stream. The measured electron density basically matches the degree of magnitude of the theoretical estimate calculation. However, the measured value of the electron temperature is higher than the estimate calculation. This is possibly because the graphic solution method is not too accurate. At the same time, as revealed by the measurement result of the electron temperature, basically the electron temperature of the test gas current is homogeneous because the measured values at various measurement points are randomly distributed within the error range of measurement. This result matches the physical characteristics. Since the electron mass is considerably smaller than the mass of ions and neutral molecules in the gas stream, during their collision process there is little exchange of energy between the electrons and these particles. Therefore, the electrons are unable to maintain energy equilibrium with other heavy particles and still maintain the energy state in front of the throttle.

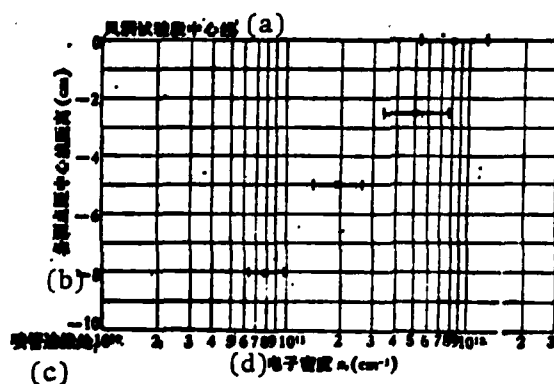


Fig. 8. Calibration result of electron density of test gas stream in H-4 electric-arc-heated wind tunnel.  
(The cross section of the gas stream is 8 cm from the exit of the nozzle; the entropy value of the wind tunnel is 2870-3250 calories per gram.)  
[Key on the following 51 page]

[Key of Fig. 8 on the preceding page]

Key: (a) Center line of testing sector of wind tunnel;  
(b) Distances (cm) of various measurement points from  
the center line; (c) At edge of nozzle; (d) Electron  
density  $n_e$  ( $\text{cm}^{-3}$ ).

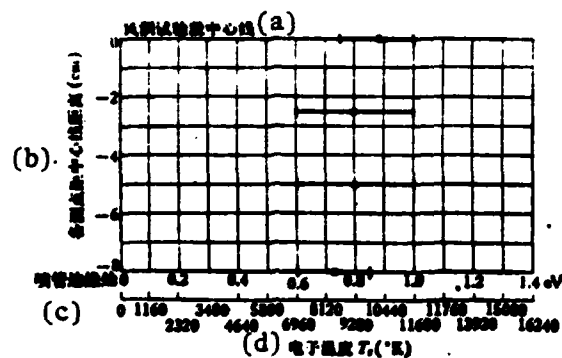


Fig. 9. Calibration and measurement results of electron temperature of test gas stream in H-4 electric-arc-heated wind tunnel: The results were totalled from three cross sections 0, 4 and 8 cm from the exit of the nozzle; the entropy value of the wind tunnel is 2400-3900 calories per gram.

Key: (a) Center line of testing sector of wind tunnel;  
(b) Distances (cm) of various measurements from center line;  
(c) At edge of nozzle; (d) Electron temperature  $T_e$  ( $^{\circ}\text{K}$ ).

The calibration-measurement testing in the second stage emphasized the distribution of measuring the electron-density cross section. Since it can be considered that within the same cross section the electron temperature is homogeneous, the variation in ion current represents the variation in electron density. Thus, the probe deviates in fixation (voltage fixed at -12 V) and the three-dimensional support can continuously move across the gas stream. In such a way, the value distribution of the saturated ion current measured is the distribution shape of the cross section of the electron density. Figure 10 shows a typical measurement curve.

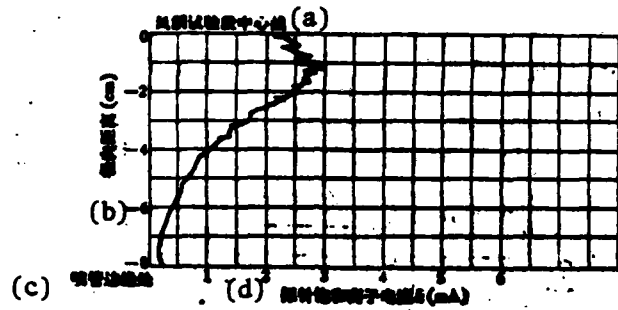


Fig. 10. Measurement curve of distribution of saturated ion-current cross section in test gas stream of H-4 electric-arc-heated wind tunnel: the curve shows the cross sectional result 15 cm from the nozzle exit.  
 Key: (a) Center line of testing sector of wind tunnel;  
 (b) Diametral distance (cm); (c) At edge of nozzle;  
 (d) Saturated ion current  $I_i$  (mA) of probe.

## V. Conclusion

The testing of calibration and measurement indicates that the iridium electrostatic probe can be operated in a high-temperature wind tunnel; the characteristics of the probe meet the testing requirements.

The electrostatic probe can be used to measure the electron density, electron temperature, and the distribution of the cross section of a gas stream tested in a wind tunnel. At the same time, results of probe measurement also provide a basis for evaluating the degree of nonequilibrium of a gas stream in a wind tunnel because the difference in degree of nonequilibrium of the gas stream in the wind tunnel can apparently be revealed in the magnitude of the electron density in the gas stream. By assuming the degree of nonequilibrium of the gas stream in the wind tunnel and calculation of electron density based on theoretical calculation, and comparing with the measured electron density, the degree of non-equilibrium of the gas stream can be determined.

## LITERATURE

1. Swift, J. D., and Schwar, M. J. R., Electrical Probes for Plasma Diagnostics, London, Iliffe (1970).
2. Laframboise, J., AD634596.